DEPARTAMENT OF PHYSICS

ANTÓNIO DE LINO DELGADO FORTES

BSc in Biomedical Engineering

SPECTROSCOPIC EVALUATION OF THE FLUORINE UPTAKE IN HUMAN ENAMEL- FLUORAPATITE OR CALCIUM FLUORIDE

MASTER IN BIOMEDICAL ENGINEERING

NOVA University Lisbon

September 2023

DEPARTAMENT OF PHYSICS

SPECTROSCOPIC EVALUATION OF THE FLUORINE UPTAKE IN HUMAN ENAMEL- FLUORAPATITE OR CALCIUM FLUORIDE

ANTÓNIO DE LINO DELGADO FORTES

Master in Biomedical Engineering

Adviser: Alda Sofia Pessanha De Sousa Moreno
Researcher, NOVA University Lisbon
Co-advisers: João Miguel Loureço Silveira
Researcher and Professor, Lisbon University

Examination Committee:

Chair: Doutor Hugo Filipe Silveira Gamboa,
Associate Professor, FCT-NOVA
Rapporteurs: Doutora Susana Isabel Conde Jesus Palma,
Researcher, FCT-NOVA
Adviser: Alda Sofia Pessanha De Sousa Moreno
Researcher, FCT-NOVA

MASTER IN BIOMEDICAL ENGINEERING

NOVA University Lisbon
September 2023

SPECTROSCOPIC EVALUATION OF THE FLUORINE UPTAKE IN HUMAN ENAMEL-FLUORAPATITE OR CALCIUM FLUORIDE

To my mother Joana Delgado
To my father Lino Fortes
To my brothers Idelson, Manuel e Wilson
To my sisters Luisa, Adelina, Luana, Delfina e Maria
To my girlfriend Jéssica Ascensão

ACKNOWLEDGMENTS

I would like to thank my adviser, Sofia Pessanha, for the guidance, professionalism, dedication, availability and trust throughout the completion of this work, without this support this work would not have been carried out.

To my co-adviser, João Silveira, for availability, attention, and support with the materials to carry out the work.

To Marta Lopes for her collaboration and advice in this work.

To my mother, Joana Delgado, my brothers, and my aunt Delfina Almeida for their support over these 5 years.

To my girlfriend, Jéssica Ascensão, for her unconditional support throughout the course and for her availability, I thank you from the bottom of my heart with love.

To my colleagues and lifelong friends, Renato Ferreira, Lenino Dias and Dalila Leonor for the support and motivation through these years.

My cousins Daniela Almeida and Dayanne Almeida for their companionship and affection.

To all my family and friends outside the university who in one way or another were part of this long journey.

To all the Professors at FCT-UNL who were involved in my study process.

To all course colleagues and especially to Gustavo Schleimann, Renato Ferreira, Mitsa Lopes, Oriza Varela, Ana Genebra, Matilde Amaro, Tatiana Santos, Margarida Barata, José Brito, Alessandro Fortes for the moments of friendship and knowledge sharing.

At the institutional level, I would like to thank the NOVA school of Science and Technology for welcoming me as an Integrated Master's student.

"You cannot teach a man anything; you can only help him
discover it in himself." (Galileo).

ABSTRACT

Based on epidemiological evidence, is estimated that around 2.4 billion people suffer from dental caries, which is a chronic infectious disease that results in the demineralization of human tooth enamel. The destruction of the calcified tissues of the tooth (dentin, enamel, and cementum) promotes the demineralization of hydroxyapatite (HAp) $Ca_{10}(PO_4)_6(OH)_2$, the main mineral in human enamel. However, the use of topical fluoride product can lead to the formation of fluorapatite (FAp) $Ca_{10}(PO_4)_6F_2$, that can be obtained from hydroxyapatite by chemically replacing hydroxide ions with fluoride ions. The lower solubility and greater mechanical strength of FAp increases the mineral's resistance to demineralization, reducing the development and prevalence of caries.

The aim of this study is to evaluate the fluorine (F) uptake on the human enamel, i.e., identify the compounds formed after application of Colgate Duraphat®, that is, the formation of FAp in human tooth enamel acts as a remineralizing agent, therefore the main objective of the study is to identify whether FAp forms in enamel in the presence of fluoride. Particle Induced Gamma Ray Emission (PIGE spectroscopy) was used to determine the concentration of F in enamel and Raman spectroscopy to analyze the vibrational modes of the phosphate ions in enamel.

In the study, 54 samples of human teeth enamel were divided in control (C, 27 samples) and tests (T, 27 samples) were evaluated. The C samples didn’t receive any treatment with fluoride, and in test, the samples were applied Colgate Duraphat, 3 times over a 12-day period, lasting 1 minute each application. The results from PIGE showed an increase in F concentrations in the tests samples compared with the control samples, i.e., an increase average of 160%, also, changes in the Raman spectra were observed: a shift in the main vibrational mode ν_1 of PO_4 was observed between C and T samples, with an average around 0.1 cm^{-1} towards the higher wavenumbers, with suggest the formation of FAp in human tooth enamel in the presence of fluoride. Machine Learning algorithms were used to further evaluate these changes, namely Random Forest Classifier to evaluate if the samples were treated or not with topic fluoride (to automatically identify the compound on the enamel) with 87.5% accuracy and using Random Forest Regressor to estimate the concentration of fluoride, however this model was less accurate ($R^2 = 0.33$).

Keywords: Dental Caries, Demineralization, Enamel, Hydroxyapatite, Fluorapatite, Raman Spectroscopy, PIGE, Random Forest Classifier, Random Forest Regressor.

RESUMO

Com base em evidências epidemiológica, estima-se que aproximadamente 2.4 mil milhões de pessoas sofrem de cárie dentária, que é uma doença infeciosa crónica que provoca a desmineralização do esmalte dentário. A destruição dos tecidos calcificados do dente (dentina, esmalte e cemento), promove a desmineralização da hidroxiapatite (HAp) $Ca_{10}(PO_4)_6(OH)_2$ que é o principal mineral constituinte do esmalte dentário humano. No entanto, o uso de produtos tópicos fluoretado pode levar a formação da fluorapatite (FAp) $Ca_{10}(PO_4)_6F_2$, que pode ser obtido a partir da HAp por substituição química dos iões hidroxilo por fluoreto. A baixa solubilidade e a maior resistência mecânica da FAp em relação a HAp, aumenta a resistência a desmineralização, reduzindo a prevalência e o desenvolvimento da cárie.

O objetivo do estudo é avaliar a incorporação de flúor no esmalte dentário, ou seja, identificar os compostos formados depois da aplicação do Colgate Duraphat® no esmalte, uma vez que, a formação de FAp no esmalte dentário humano age como um agente remineralizador, portanto o objetivo principal do estudo é identificar se forma a FAp no esmalte na presença de flúor. A técnica de Emissão de Radiação Gama Induzida por Partículas (espetroscopia PIGE) foi usado para determinar a concentração de flúor no esmalte das amostras, e a espetroscopia Raman foi usado para analisar os modos vibracionais dos iões fosfato no esmalte.

No estudo foi avaliado 54 amostras de dentes, divididos em grupo de controlo (C) com 27 amostras e grupo de teste (T) com 27 amostras também. O grupo C não recebeu nenhum tratamento com flúor, e no grupo de teste foi aplicado Colgate Duraphat ,3 vezes num período de 12 dias, com duração de 1 minuto cada aplicação. Os resultados obtidos pelo PIGE demonstraram um aumento da concentração de flúor nas amostras de teste em comparação com as amostras de controlo, ou seja, um aumento médio de 160%, também se observou alteração nos espetros Raman entre os 2 grupos. Houve um desvio no modo vibracional ν_1 do PO_4 entre as amostras de C e T, com uma média de 0.1 cm^{-1} em direção aos números de onda mais altos, o que sugeriu a formação da FAp no esmalte na presença de flúor. Algoritmos de Machine Learning foram usados para avaliar melhor estas alterações, nomeadamente o classificador Random Forest para avaliar se as amostras receberam tratamento ou não com flúor (para identificar os compostos formado no esmalte) com uma precisão de 87.5%, e o Random Forest

Regressor foi usado para estimar a concentração de flúor nas amostras, no entanto, este modelo foi menos preciso ($R^2 = 0.33$).

Palavas chave: Cárie dentária, Desmineralização, Esmalte, Hidroxiapatite, Fluorapatite, Espetroscopia Raman, PIGE, Classificador Random Forest, Regressor Random Forest.

CONTENTS

LIST OF FIGURES

LIST OF TABLES

ACRONYMS

AI	Artificial Intelligence
CNA	National Accelerator Center
CRM	Certified Reference Materials
DEJ	Dentin-Enamel Junction
DR	Depolarization Ratio
EDXRF	Energy Dispersive X-ray Fluorescence
FAp	Fluorapatite
FCT	Faculdade de Ciências e Tecnologia
FHAp	Fluorhydroxyapatite
FMDUL	Faculdade de Medicina Dentária Universidade de Lisboa
FTIR	Fourier-Transform Infrared Spectroscopy
GBR	Gradient Boosting Regressor
HAp	Hydroxyapatite
HPGe	Hyper Pure Germanium
LIBPhys-UNL	Laboratório de Instrumentação, Engenharia Biomédica e Física das Radiações- Universidade Nova de Lisboa
LR	Logistic Regression
ML	Machine learning
NEC	National Electrostatics Corporation
NIST	National Institute of Standards and Technology
PCA	Principal Component Analysis
PIGE	Particle Induced Gamma Ray Emission
RF	Random Forest

RFR	Random Forest Regressor
RS	Raman Spectroscopy
SVR	Support Vector Regression

SYMBOLS

A	Target nuclei
B^*	Excited nuclei
C_{CRM}	Certified reference materials concentration
C_{sample}	Sample's concentration
Ca_2	Calcium
Ca^{2+}	Calcium ions
CaF_2	Calcium fluoride
$Ca_{10}(PO_4)_6(OH)_2$	Hydroxyapatite chemical formula
$Ca_5(PO_4)_3F$	Fluorapatite chemical formula
Cl^-	Chlorine ion
CO_3^{2-}	Carbonate ion
Cu^{2+}	Copper ion
E	Electric field intensity
Eb	Energy of the bombardment beam
Er	Resonance energy of the nuclei
E_F	Proton energy beam
E_o	Vibrational amplitude of the laser
F	Fluorine
F^-	Fluoride
Fe^{2+}	Iron ion
H	Hydrogen
H^+	Hydrogen ion
$H_2PO_4^-$	Dihydrogen phosphate ion
H_3PO_4	Phosphoric acid
He	Helium
HPO_4^{2+}	Hydrogen phosphate ion
I	Incident particle current
K^+	Potassium ion

Mg^{2+}	Magnesium ion
Mn^{2+}	Manganese ion
N	Number of target nuclei per unit area
Na^{+}	Sodium ion
NH_4^{+}	Ammonium ion
Ni^{2+}	Niquel ion
OH^{-}	Hydroxide ions
P	Induce electric dipole
PO_4	Phosphate
$PO_4{}^{3-}$	Phosphate ions
R	Production rate of gamma particle
S	Total stopping power
S_{CRM}	Sample's stopping power of certified reference material
S_{ele}	Electron stopping power
S_{nuc}	Nuclear stopping power
S_{sample}	Sample's stopping power
SO_4^{2-}	Sulfate ion
v_m	Molecular vibration frequency
v_0	Laser frequency
v_1	Symmetrical stretching vibrational mode of phosphate ion
v_2	Symmetrical angular deformation mode of phosphate ion
v_3	Antisymmetric stretching vibrational mode of phosphate ion
v_4	Asymmetrical angular deformation mode of phosphate ion
Y_{CRM}	Certified reference material's net peak areas
Y_{sample}	Sample's net peak areas
Z	Atomic number
Zn^{2+}	Zion ion
$\varepsilon(E)$	Effective stopping section
$\parallel$	Parallel
$\perp$	Perpendicular

1

INTRODUCTION

1.1 Background and motivation

Tooth decay is a chronic infectious disease that results in the demineralization of tooth enamel, which has been affecting the oral health of millions of people around the world [1]. Based on epidemiological evidence, it is estimated that approximately 2.4 billion people suffer from dental caries diseases [2], [3].

Tooth decay consists of the destruction of the calcified tissues of the tooth (dentin, enamel and cementum), through the attack of acids produced by bacteria present in the mouth (mainly *Streptococcus mutans*) [4], which metabolize carbohydrates and produce acids as by-products, thus leading to a decrease in pH in the oral cavity, causing demineralization of the minerals that make up tooth enamel (calcium and phosphate). In turn, to produce an erosive lesion, the following three stages must occur: loss of protective substances in saliva, dissolution of the mineral on the tooth surface and destruction of the tooth surface [4]– [6].

Tooth erosion begins with the demineralization of the surface layers of enamel and can progress to significant loss of tooth structure. The acids responsible for dental erosion can be intrinsic or extrinsic [6]. While extrinsic factors are related to eating habits (use of carbohydrates) and lifestyle, intrinsic factors can be caused by systemic diseases [6]. In this context, direct exposure to acids in the oral cavity promotes the demineralization of hydroxyapatite $Ca_{10}(PO_4)_6(OH)_2$ (HAp), due to the sub saturation of minerals in relation to the surrounding microenvironment [7].

Saliva plays an essential role in the bioavailability of calcium (Ca^{2+}) and phosphate ($PO_4{}^{3-}$) ions for the dental remineralization process, however, frequent exposure to acids can overcome the protective effect of saliva, causing demineralization of the HAp structure. To reverse this process, it is necessary to use topical remineralizing agents that contain calcium, phosphate and especially fluoride [7].

The use of topical fluoride agents in the prevention of dental caries is widely studied, and was demonstrated in several studies [7]–[11], that the use of fluoride can lead to the formation of fluorapatite $Ca_{10}(PO_4)_6F_2$ (FAp), that can be obtained from HAp by chemically replacing hydroxide ions (OH^-) with fluoride (F^-). The lower solubility and greater mechanical strength of FAp compared to HAp increases the mineral's resistance to demineralization, thus reducing the development and prevalence of caries [11].

However, the large number of ionic species present in saliva such as calcium, can interfere with the formation of FAp, because they can react with fluoride and give rise to other by-products, mainly calcium fluoride (CaF_2). In general, regardless of the efficacy of fluoride in *in vitro* studies, clinical results are mostly below expectations and are mainly due to the lack of reliable methods for assessing the formation of FAp in enamel, i.e., for unequivocally assessing fluoridation in *in vitro* tests, which would make it possible to select the most promising materials for clinical tests and the development of efficient tooth fluoridation materials [11].

Many methods based on different techniques have been proposed to assess the mineral content of teeth. Microhardness, microradiography, electron backscatter imaging and quantitative light-induced fluorescence are techniques used to estimate mineral content, but they cannot distinguish between different mineral compounds [2], [11], [12]. Other methods can distinguish between CaF_2 and FAp, but need to dissolve the sample, and thus destroy the tooth [2]. Raman spectroscopy has been used extensively to study the vibrational modes of pure apatite $Ca_5(PO_4)_3(OH, F, Cl)$, and the literature suggests that the formation of FAp can be assessed using Raman spectroscopy by a measurement of the shift in the symmetric phosphate stretching band to higher wavenumbers [2], [13].

Previous studies evaluated tooth samples after treatment with products containing F. The increase in fluoride in the teeth was evident in measurements using *Particle Induced Gamma Ray Emission* (PIGE) [14], [15]. However, they didn’t measure variations in the band energy of the symmetrical stretching vibrational mode of phosphate (v_1) by Raman spectroscopy (RS) because of the low sensitivity to the degree of substitution of F in the HAp structure [10], [11]. Also, it can be due to the lack of energy resolution of the system used or interference from the ionic species present in human saliva interfering in the formation of FAp leading to other by-products, such as calcium fluoride (CaF_2), the study being the continuation of the thesis carried out by Dias.Kateline, in 2020 [15] .

Raman spectroscopy has been widely used to study apatites, as it is a non-destructive technique and provides valuables information of the structure, chemical composition and vibrational modes of these materials. This technique can be used to discriminate between the compounds formed in teeth after the use of topical fluoride products, i.e., it can be used to discriminate between HAp and FAp, and a study carried out in 2010 [13] showed a shift in the wave number of the v_1 vibrational mode of phosphate in HAp in relation to FAp of approximately 3 cm^{-1}, due to the replacement of HO^- ions by F^-. It is therefore possible to extract a set of characteristics from the Raman spectra that make it possible to distinguish the minerals formed in the dental enamel in the study. This evaluation can be aided by Machine Learning tools, to classify the minerals present in the dental enamel (HAp, CaF_2 or FAp) in an automated way, but also as a regression problem, to study the concentration of fluoride present in the tooth samples.

1.2 Objective and plan of the dissertation

This study aims to evaluate how F incorporate into the HAp matrix, i.e., to identify the compounds formed in the tooth enamel (FAp, CaF_2 or other) after using Colgate Duraphat®, used for caries prophylaxis (tooth cleaning) and the treatment of hypersensitive teeth.

The work plan included the use of PIGE technique to evaluate the incorporation of fluoride into the teeth, and then Raman spectroscopy to evaluate the vibrational modes of the minerals present in the samples, to identify the compounds formed.

To achieve the main goal of the study, the following tasks were carried out:

- Development of an *in vitro* model for the application of Colgate Duraphat® in the dental specimens.
- Evaluate the incorporation of fluoride, i.e., determine the concentration of fluoride in the tooth specimens using the PIGE technique.
- To analyze the chemical composition of dental enamel, i.e., to identify and compare the vibrational modes of phosphate in the Raman spectra.
- To develop Matlab codes for the pre-processing and extraction of essential features from the data obtained by Raman spectroscopy and the PIGE technique.
- Use the extracted features to develop a classification and regression model in Machine Learning.

1.3 Dissertation Structure

In addition to this chapter, this dissertation is divided into 5 more chapters. Chapter 2 summarizes the theoretical concepts needed to understand oral biology in the process of fluoride incorporation into tooth enamel.

Chapter 3 presents a summary of the state of the art and the studies that have already been carried out to evaluate the incorporation of fluoride into tooth enamel.

Chapter 4 will briefly present the theoretical concepts of the RS and PIGE analytical techniques essential for the analysis of the samples under study.
Chapter 5 presents the materials and methods used to apply Colgate Duraphat® to the tooth specimens. Finally, Chapter 5 analyzes and discusses the results obtained in the study.

“The research work described in this dissertation was carried out in accordance with the norms established in the ethics code of Universidade Nova de Lisboa. The work described and the material presented in this dissertation, with the exceptions clearly indicated, constitute original work carried out by the author.”

2

THEORICAL CONCEPTS

This chapter presents the concepts needed to understand oral biology and the process of fluoride uptake into tooth enamel.

2.1 The Tooth

The human tooth is made up of a visible part, called the crown, and a part implanted in the dental alveoli called the root, the two regions being delimited by the neck of the tooth [1], [16], showed in figure 2.1.

The center of the tooth is called the pulp cavity and is filled with a cluster of blood vessels, nerves and connective tissue called the pulp. The pulp cavity is surrounded by dentin, a type of cellular tissue similar to bone [1], [17]. The dentin of the tooth crown is covered by a rigid, acellular substance called enamel, which protects the tooth from acid erosion and mechanical wear [17]. In the root region, the surface of the dentin is covered by cementum, a type of mineralized and avascular connective tissue, which covers the root of the tooth, the attachment of the tooth is due to the periodontal ligaments which consist of fibrous connective tissue that extends through the alveolar walls and attaches to the cementum [1], [12], [17].

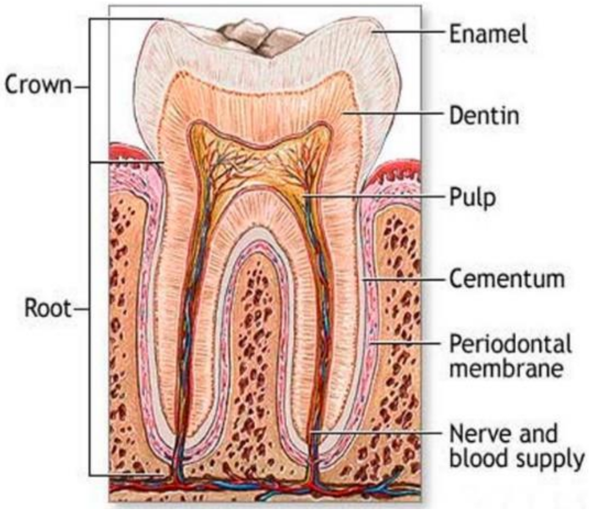

Figure 2.1-Anatomical and structural representation of the human tooth. Adapted from [1].

2.1.1 Tooth enamel and its composition

Human tooth enamel is formed by the synthesis and secretion of proteins by the ameloblasts and plays an essential role in protecting the inner layers of teeth against mechanical and chemical actions [2]. It is the hardest and most highly mineralized tissue in the human body, with a composition of up to 96-97% by weight inorganic matter, 2-3% water and only 1% organic matter (proteins) [2].

HAp, in the form of a crystalline network, is the largest mineral constituent with around 90% to 92% by volume; other elements such as fluoride, carbonate, magnesium, sodium, chloride, potassium and zinc are present in smaller quantities. The other constituents of tooth enamel include proteins from the organic matrix with around 1% to 2% by volume and water with approximately 2% to 3% by volume [5], [7].

Tooth enamel is considered a biologically dead tissue, but it is permeable and allows ion exchange with the oral cavity environment, particularly saliva. The HAp molecule is susceptible to replacement of the Ca^{2+} cation by K^{+}, Na^{+}, NH_4^{+}, Mn^{2+}, Ni^{2+}, Cu^{2+}, Mg^{2+}, Fe^{2+} or Zn^{2+}, the OH^{-} group by F^{-} and Cl^{-} , and PO_4^{3-} group by CO_3^{2-}, SO_4^{4-}, SO_4^{2-} [6], [8].

Ion substitution leads to changes in the properties of apatite: substitution by F^{-} decreases crystal solubility, substitution by CO_3^{2-} is associated with a decrease in crystallinity and an increase in solubility, and magnesium inhibits crystal growth [6], [8]. However, after substitution and absorption of these ions in the enamel, its structural configuration remains almost unchanged.

2.1.2 Structure and properties

Tooth enamel is organized mainly in the form of HAp crystals and has an acellular and avascular structure, without the ability to regenerate or repair itself. These characteristics reflect the processes, which occur during enamel formation [5], [9].

Structurally, HAp crystals are arranged in three levels of hierarchical organization, which explains their mechanical strength [5]. At the highest structural level, the bundles combine dozens of enamel rods, forming the Huter-Schreger bands (HSB), which is approximately 50 μm wide, and is related to the different refractive properties of light in prisms of adjacent layers [5]. At the next level the enamel rods (prismatic and interprismatic) which represent the primary and fundamental structural units, are cylindrical structures 5-8 μm in diameter, running from the dentin-enamel junction (DEJ) to the outer enamel surface [5]. At the last structural level, the nanoscale, each HAp molecule in the maturing enamel has a hexagonal geometry, and the repetition of the compound allows the formation of crystals of different sizes [5], [9], [10].

Tooth enamel has an average Young's modulus of approximately 80 GPa, while dentin, which acts as a support, is less fragile and less mineralized than enamel, thus having a Young's modulus of approximately 20 GPa [16]. However, the mechanical properties of enamel vary throughout its depth, its surface being more rigid, dense and less porous than its interior.

In terms of solubility, the lower enamel surface is more sensitive to external acids and dissolves phosphate at a higher rate than the outer surface [12], [17]. This is related to the fact that the F ions preferentially bind to the free enamel surface, thus replacing the hydroxyl groups on the HAp crystals, producing fluorhydroxyapatite (FHAp) or FAp, which has a lower average solubility than HAp [17].

2.2 Dental enamel erosion

Erosion is the process by which hard dental tissues are destroyed by the action of an acid of an endogenous or exogenous nature that occurs on the enamel surface, involving more rapid and comprehensive dissolution, leading to progressive enamel loss over the long term. It occurs without the intervention of microorganisms and depends on the structure of the tooth and its interaction with the soft tissues, tongue and gingiva [19], [20]. Dental caries results from the demineralization of the innermost layer of enamel through the attack of acid produced by bacteria present in the mouth (mainly *Streptococcus mutans*) [4], which metabolize carbohydrates and produce acids as by-products, leading to the dissolution of HAp when the pH decreases in the excessive presence of H^+ ions [20], [21]. However, to produce an erosive lesion, the following three stages must occur: loss of protective substances in the saliva, dissolution of the mineral on the tooth surface and destruction of the tooth surface due to chemical action [4]– [6].

Saliva plays an important role in dental erosion, as it acts as a semi-permeable barrier to protect the enamel, since it has a buffering effect, preventing changes in the pH of the oral cavity, as it contains various ions, such as phosphate and calcium, without which dental remineralization would not be possible [7].

2.2.1 Effect of pH on enamel erosion

Exposure of the oral cavity to acids causes HAp to dissolve according to the following equation (2.1) [16], when pH values are lower than the critical value, which is around 5.5, and this value can vary depending on the concentration of calcium and phosphate ions in solution [17].

$$Precipitation \leftrightarrows Dissolution$$

$$Ca_{10}(PO_4)_6\,(OH)_2 \leftrightarrows 10Ca^{2+} + 6{PO_4}^{3-} + 2OH^- \qquad (2.1)$$

$$Solid \leftrightarrows Solution$$

HAp dissolves, releasing ions of Ca^{2+}, PO_4^{3-} and OH^-, and the reaction continues until the solution is saturated in relation to HAp, i.e., when the reaction in the forward direction (dissolution) comes into equilibrium with the reaction in the reverse direction (precipitation) [22], [23].

There are 2 reasons for the increase in the solubility of tooth enamel when it comes into contact with acidic substances:

- The first is related to the high concentration of hydrogen ions (H^+) in the solution, which react with the OH^- ions to form water, according to the following chemical reaction:

$$H^+ + OH^- \leftrightarrow H_2O \qquad (2.2)$$

The product of the concentrations of the ions H^+ and OH^- in water is a constant, whose value is 10^{-14} $(mol/L)^2$, so as the $[H^+]$ increases in acidic solutions, the $[OH^-]$ will decrease.

- The second is due to the fact that inorganic phosphate in saliva is present in 4 different forms, HPO_4^{2-}, PO_4^{3-} , H_3PO_4 and $H_2PO_4^-$, where the proportions depend entirely on pH, as illustrated in figure (2.2) [23].

Figure (2.2) illustrates how the proportions of the 4 phosphate species vary with pH when the total phosphate concentration is $5 \times 10^{-3}\, mol/L$, as is typical of saliva [23]. The lower the pH, the lower the concentration of PO_4^{3-}, the only species that contributes to the precipitation of HAp in the enamel [23].

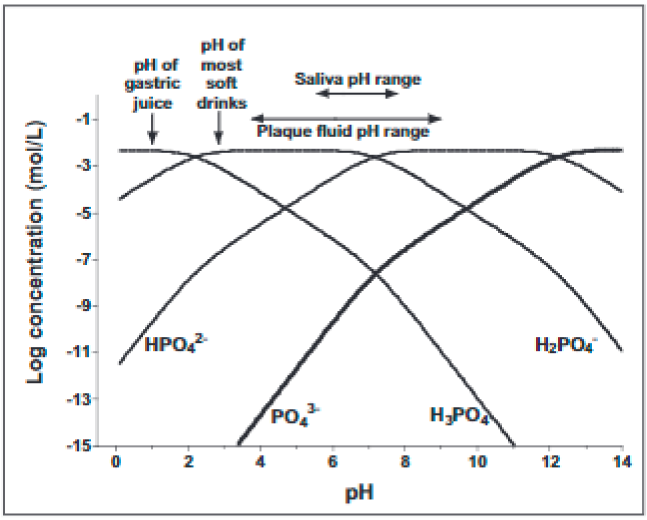

Figure 2.2- Variation of the PO_4 concentration as a function of ambient pH. Adapted from [23].

Saliva is considered one of the most important biological factors in determining the intraoral neutralizing effects of acid exposure. In addition to its antibacterial and cleansing action, it acts as a constant source of calcium and phosphate that keeps the oral cavity super-saturated in relation to enamel minerals, thus inhibiting tooth demineralization in low pH situations, and promoting tooth remineralization when the pH returns to a neutral state [17], [23]. On the other hand, the organic components promote the formation of a protective surface film, made up of salivary proteins, which promotes the diffusion of calcium and phosphate for remineralization [22]–[24]. However, there is an erosion threshold due to the action of acids, after which the enamel cannot be remineralized, due to the loss of the matrix necessary for the growth of crystals and acquires a bacterial film that inhibits the deposition of mineral in the enamel, even under conditions of saliva supersaturation in relation to the constituent elements of the tooth [17].

2.2.2 Effect of fluoride on enamel erosion

The absorption of fluoride in tooth enamel is an effective defense against caries since it improves the remineralization of initial carious lesions and protects the oral cavity against new carious attacks [25]. When fluoride solutions in low concentrations are applied to the enamel, the F ions replace the OH ions in the HAp structure, thus forming FHAp and FAp, which are less soluble and more resistant to demineralization than the original or calcium-deficient HAp [23], [25]–[27]. In the presence of a high concentration of fluoride, the formation of a layer of calcium fluoride (CaF_2) is promoted in the teeth, which constitutes a reservoir of F that releases F when the pH of the environment drops [25], [27], [28].

Due to the smaller atomic radius of F compared to OH, F occupies the most symmetrical position possible in the gap left by OH in the HAp structure, allowing a reduction of around 1% in the volume of FAp compared to HAp, which explains its greater mechanical strength and lower solubility [25], [27]. The low solubility allows the mineral to precipitate more quickly in contact with solutions containing calcium and phosphate, so the incorporation of fluoride into the enamel acts as a catalyst for the remineralization process [25].

The critical demineralization pH of FAp is 4.5, it is significantly lower than that of HAp, 5.5, thus reducing susceptibility to erosion in low pH environments [25], [26]. Also, in the presence of fluoride, saliva is supersaturated with respect to FAp for most physiological pH values, whereas supersaturation with respect to HAp is restricted to pH values above 5.5, thus making FAp precipitation favorable in the presence of the F ion [2], [17].

3

LITERATURE REVIEW ON FLUORINE UPTAKE IN DENTAL ENAMEL

The first study on the effect of fluoride on tooth enamel was conducted by dentist Dr. Frederick McKay [29], [30], at the beginning of the 20th century, when he noticed that many of his patients had whitish stains on their teeth. They discovered that the high concentration of fluoride in the local water supply was the main cause of the appearance of the stains, however, they noticed that the patients with stains had less dental caries than those without stains, thus raising the hypothesis that fluoride could have a protective effect on tooth enamel [30].

One of the first studies about the formation of FAp in enamel was carried out by Dean et al. in the 1950s [30]–[33]. In 1983, a study by Dijkman et al. [34], demonstrated that CaF_2 was stored on the enamel surface for weeks or months under neutral pH conditions, thus relating the composition of the enamel to the pH of the medium. Using electron microscopy, Duschner et al. [34], in 1997 demonstrated that the CaF_2 precipitate is not only formed on the tooth surface, but also appears as a granular material in the enamel to a depth of around 40 μm [34]. Based on previous studies, it has been shown that demineralized enamel is able to absorb more fluoride than non-demineralized tooth surfaces according to Hellwig et al. [34].

More recently, a study carried out in 2010 by M. Campillo et al. [13] using Raman spectroscopy, showed that the hydroxyl ions in the HAp structure can be partially or totally replaced by fluorine, forming FHAp or FAp. A study published in 2017 by K. H. Akkus et al. [35], showed that incorporating fluoride into dental enamel increased the amount of FAp and decreased the amount of HAp.

Changes in enamel are assessed using various techniques, such as microhardness testing, to evaluate the mechanical strength of teeth, and electron microscopy to evaluate the enamel morphology [13]. But there are also various spectroscopic methods used to assess fluoride in enamel, such as Raman spectroscopy, Energy Dispersive X-Ray Fluorescence (EDXRF) technique, PIGE, and Fourier Transform InfraRed spectroscopy FTIR [13].

Regarding Raman spectroscopy method, there are several studies in which it is used to assess the composition of enamel. The fluoride ions in the enamel create specific bands that can be used to detect and quantify the absorption of fluoride in the enamel.

Polarized Raman spectroscopy was first applied by Ko et al. [36] in 1999 to analyze the enamel, concluding that the change in the orientation of the molecular bonds of the enamel structure in demineralized regions can be quantified by observing the increase in the ratio between the intensity of the scattered light in relation to the direction of polarization of the incident light, and by the decrease in anisotropy (directionality of polarization) in the range of intensities of the phosphate band in the Raman spectrum of polarized light.

To measure F absorption in enamel during mineralization and demineralization cycles using fluoride-containing products, Komatsu et al. [37] used the PIGE technique to quantify the incorporation of fluoride into the enamel, thus evaluating the concentration of fluoride in the enamel. Arshed et al. [38], used the technique to calculate the distribution of F in two-millimeter-thick layers of enamel from 8 tooth samples, measuring in different zones, and made it possible to estimate the concentration of F, which ranged from 81 to 800 ppm for different samples.

More recent studies related to the incorporation of fluoride into tooth enamel, carried out by Dias K. in 2020 [15], [39] , showed the absorption of fluoride in dental enamel and other carried out by Otel, et al. in 2020 [40], investigate the protective suitability of a dental fluorinated varnish by means of X Ray fluorescence and Raman spectroscopy, but it was not possible to identify which compounds formed in the hydroxyapatite matrix.

Raman spectroscopy has been applied in various fields of study, as it is a non-invasive and non-destructive technique, making it a powerful and essential technique in many studies. However, spectral data is often complex and contains random noise, requiring additional processing to extract the necessary information. Today, with the advance of artificial intelligence (AI), machine learning (ML) algorithms have become an effective tool in the analytical sciences, which can be used to analyze complex RS datasets. In more recent studies, ML has been used to pre-process RS spectral data, optimizing computational processing time and pre-processing results according to Bocklitz et al. 2011 [41], [42]. ML is also used to identify patterns and connections in the dataset, as well as perform classifications in a more efficient way than traditional methods according to Qi et al. 2023 [42].

4

ANALYTICAL SPECTROSCOPY TECHNIQUES

This chapter includes the basic physical principles involved in the analytical spectroscopic techniques used.

4.1 Raman spectroscopy

Raman scattering was discovered in 1928 by Chandrasekhra Venkata Raman [43], It is a non-destructive technique that allows the identification of the vibrational modes present in a sample for the determination of its chemical composition and molecular structure [44], [45].

4.1.1 Vibrational modes

Molecular vibrations are movements of atoms in a molecule that occur from changes in the distance or angle in the chemical bonds. Each molecular vibration is described by the fundamental frequency associated with each type of vibrational movement [43].

A molecule can have several vibrational modes depending on its molecular configuration. The stretching mode corresponds to a variation in the distance between the atoms and can be symmetric (the atoms involved in the vibration move in the same direction, moving apart and coming together in synchrony) or antisymmetric (the atoms involved in the vibration move in opposite directions, one moving away and the other coming together). But there is also the deformation mode which corresponds to the angular variation, which includes bending, i.e. changing the angle between the bonds; rocking which corresponds to the oscillation of the atoms in the molecule; scissoring, i.e. the atoms move in opposite directions (opening and closing); wagging when the atoms in a molecule move up and down; and finally, twisting which occurs when the atoms rotate around a central bond. [46], [47].

The vibrational modes of the PO_4^{3-} ion and the symmetrical stretching vibrational mode (ν_1) of the CO_3^{2-} ion represent the inorganic phase of tooth enamel. However, for this study, the molecule of interest is PO_4^{3-}, which has a symmetrical (ν_1) and antisymmetrical (ν_3)

stretching mode and symmetrical (v_2) and asymmetrical (v_4) angular deformation mode [47], [48].

4.1.2 Physical principles of Raman spectroscopy

Radiation can be scattered in two ways, through Rayleigh scattering, where the scattered beam has the same frequency v_0 as the incident beam, or through Raman scattering where the beam is scattered with a frequency $v_0 \pm v_m$, where v_m corresponds to the vibrational frequency of a molecule, interpreted as a change in the frequency (energy) of the incident beam, and the lines $v_0 - v_m$ and $v_0 + v_m$ are called Stokes and anti-Stokes lines [43].

When a molecule is excited with an electric field of intensity (E), it undergoes distortion, since the positively charged nucleus are attracted to the negative pole and the electrons to the positive pole, generating a charge separation that produces an induced electric dipole (P) [43], given by the following equation:

$$P = \alpha E = \alpha E_0 \cos(2\pi v_0 t) \tag{4.1}$$

Where α is the polarizability, which refer to the tendency of matter, when subjected to an electric field, to acquire an electric dipole moment in response to this applied field, i.e., it is defined as the degree of deformation of a bond. Where E_0 is the vibrational amplitude of the laser and v_0 is its frequency [43].

If the molecule vibrates with a frequency v_m, for a small vibration amplitude, α is a linear function of the displacement (x) [43], which can be written by:

$$\alpha = \alpha_0 + \left(\frac{\partial \alpha}{\partial x}\right)_0 x_0 + \cdots \tag{4.2}$$

Where x_0 is the vibrational amplitude of the displacement, α_0 is the polarizability at the equilibrium position and $(\partial\alpha/\partial x)_0$ the rate of change in relation to the displacement x [43].

Expanding the polarizability in Taylor series and using trigonometric properties, we can express P as follows:

$$P = \alpha_0 E_0 \cos(2\pi v_0 t) + \frac{1}{2}\left(\frac{\partial \alpha}{\partial x}\right)_0 \alpha_0 E_0 [cos(2\pi(v_0 + v_m)t) + cos(2\pi(v_0 - v_m)t)] \tag{4.3}$$

According to classical theory, the first term represents an oscillating dipole that radiates light of frequency v_0 (Rayleigh scattering), while the second term corresponds to Raman scattering of frequency $v_0 + v_m$ (anti-Stokes) and the third term corresponds to frequency Raman scattering $v_0 - v_m$ (Stokes) [43]. The equation shows that if $\left(\frac{\partial\alpha}{\partial x}\right)_0$ is equal to zero, Raman scattering does not occur, since the second and third terms are equal to zero.

From a quantum point of view, Raman scattering can be explained by energy transitions involving the vibrational, rotational, and electronic energy levels of molecules [43], [49]. Therefore, if the photon energy is not sufficient to excite the molecule to a higher electronic state, it absorbs the photon and is excited to a virtual energy level. From the virtual state, the molecule relaxes to a lower energy state by emitting a photon.

If the electron transitions to the ground state, the incident photon and the scattered photon have the same energy and Rayleigh scattering occurs. If the transition involves an excited vibrational state, Raman scattering occurs. If the molecule is initially in the fundamental vibrational state, Raman Stokes scattering occurs, while if it is in an excited vibrational state, anti-Stokes scattering occurs, as illustrated in figure 4.1 [43], [49], [50]. Most molecules are in the ground state at room temperature, so the Raman Stokes lines is more intense than the anti-Stokes lines.

Raman spectroscopy measures the energy difference between the incident photon and the scattered photon, and as anti-Stokes scattering has less intense peaks than the peaks corresponding to Stokes scattering, Raman equipment only considers the Stokes region of the spectrum [43].

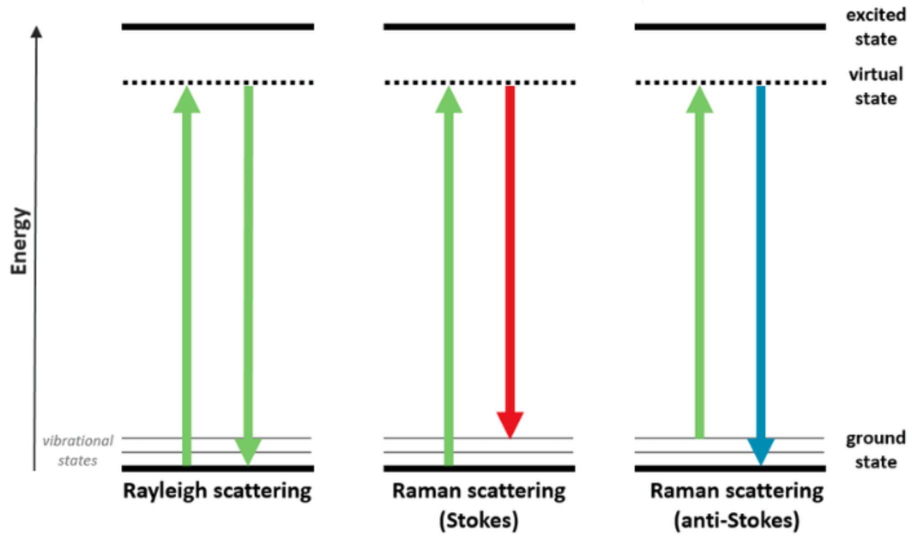

Figure 4.1- Diagram of the transitions associated with Rayleigh scattering, Raman Stokes scattering and Raman Anti-Stokes scattering. Adapted from [50].

The depolarization ratio (ρ) is a measure of the ability of enamel to reflect, absorb, or transmit polarized light. It provides valuable information on the vibrational symmetry and orientation of the molecules in a sample, allowing the organization and crystallinity of the sample be identified [43].

$$\rho_{959} = \frac{I_{959}\ (\perp)}{I_{959}\ (||)} \tag{4.4}$$

Where, I_{959} ($\perp$) and I_{959} (||) are related to the peak's intensity at 959 cm^{-1} in the Raman spectrum (v_1 (PO_4^{3-})), using perpendicular and parallel polarization between the incident and scattered radiation by the sample.

For healthy enamel, the peak corresponding to the symmetric vibrational mode v_1 of phosphate at 959 cm^{-1} is anisotropic. The spectra of damaged enamel show low dependence on the polarization of the radiation. These differences can be quantified through the quotient between the intensities of the peaks at this wavelength obtained with perpendicular and parallel polarization relative to the excitation laser.

4.2 Particle-induced gamma ray emission (PIGE)

Gamma radiation results from the decay of atomic nuclei from one excited level to another of lower energy, and in the disintegration of radioactive isotopes [51], [52]. It was discovered by the French chemist and physicist Paul Villard in 1900 while studying the radiation emitted by the element radium and classified as gamma rays by Rutherford in 1903 [51].

4.2.1 Nuclear reactions

The interaction of a particle beam with the target can occur with the electrons or the nucleus of the sample. The most likely collisions occur between the incident particle and the target's electrons, with the interaction taking place through Coulomb forces. When the collision occurs with the target's nucleus, scattering (Coulomb or Rutherford) or interaction with the nuclear potential can occur, which can lead to a nuclear reaction. As the energy of the particles increases, interaction with the target's nucleons can also occur [53]–[57].

Nuclear resonance reactions occur when an atomic nucleus absorbs a charged particle with specific energy (proton), causing nuclear excitation of an element, inducing transitions to higher energy states, subsequently with the nuclei de-excitation, emission of radiation occurs.

There are three types of resonance reactions that can lead to the emission of gamma rays:

- **Radiative capture:** the projectile (p) is captured by the target nucleus A and a B^* nucleus is formed in an excited state. The nucleus in the excited state decays to the ground state B by emitting gamma radiation.
- **Inelastic scattering:** occurs when there is no change in the particles, but the target remains in an excited state and the projectile is scattered with a different energy. Gamma radiation is emitted by de-excitation of the excited nucleus.
- **Collisions with rearrangement:** occurs when particles collide and interact in such a way that the internal states of these particles are altered during the collision. This results in a reorganization of the particles involved, often producing new particles or final states that are different from the initial states of the particles.

For the analysis of light elements by PIGE, proton-induced nuclear resonance reactions are often the most used, due to the availability of suitable bombardment energies to achieve the specific resonances of these elements, since most light elements register resonance by (p, γ) or (p, $\alpha\,\gamma$) reactions, as showed in table 4.1 [53], [58].

Table 4.1- Summary of nuclear reactions that occur with gamma radiation emission.

Radiative capture	$p + A \rightarrow B^* \rightarrow B + \gamma$	(p,γ)
Inelastic scattering	$p + A \rightarrow A^* + p' \rightarrow A + p' + \gamma$	$(p,p'\gamma)$
Collision with rearrangement	$p + A \rightarrow B^* + b \rightarrow B + b + \gamma$	$(p,\alpha\,\gamma)$

4.2.2 Cross section

Charged particles interact continuously via Coulomb force with the electrons of the medium they pass through and with the atom's nuclei. The direction of the particles changes randomly, so the probability of an interaction occurring can be expressed in terms of the effective cross-section, defined by:

$$\sigma = \frac{R}{IN} \tag{4.5}$$

Where R is the gamma particle production rate, I is the incident particle current and N is the number of target nuclei per unit area.

However, the gamma radiation resulting from resonance nuclear reactions is emitted according to a given angular distribution $r(\theta,\varphi)$, dependent on the scattering angles θ and φ, and the solid angle of the detector, $d\Omega$, is small. Thus, only a small fraction of the gamma particles emitted are detected, according to the following equation (figure 4.2).

$$dR = r(\theta,\varphi)\,\frac{d\Omega}{4\pi} \tag{4.6}$$

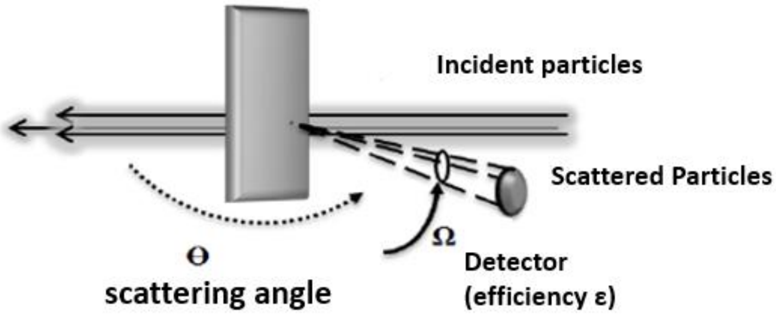

Figure 4.2- Schematic representation of the geometry of particle collisions with the target. Adapted from [58].

The differential effective cross-section $\frac{d\sigma}{d\Omega}$ is given by:

$$\frac{d\sigma}{d\Omega} = \frac{r(\theta,\varphi)}{4\pi I N} \tag{4.7}$$

The total effective cross-section results from integrating the differential effective cross-section for all angles, where $d\Omega = sen(\theta)\,d\theta\,d\varphi$ in spherical coordinates:

$$\sigma = \int_{4\pi} \frac{d\sigma}{d\Omega}\,d\Omega = \int_0^{2\pi}\int_0^{\pi} \frac{d\sigma}{d\Omega} sen(\theta) d\theta\, d\varphi \tag{4.8}$$

Knowledge of the effective cross-section for a given energy interval is fundamental for calculating the concentration of F in a thick sample using PIGE [58].

4.2.3 Stopping power

The interaction of the projectile with the target can be between the incident particles and the electrons (electron stopping power, S_{ele}), called Coulombian interaction, or interaction with the nuclei of the target's atoms (nuclear stopping power, S_{nuc}), so the total stopping power is given by:

$$S = S_{ele} + S_{nuc} \tag{4.9}$$

The stopping power translates into the loss of energy (dE) per unit length (dx) of an incident particle when it crosses the target due to interaction with it.

$$S = -\frac{dE}{dx} \tag{4.10}$$

As the stopping power depends on the thickness of the target and not on the atomic surface density, it is preferable to use the defined effective stopping section, defined by the expression:

$$\varepsilon(E) = \frac{S}{N} \tag{4.11}$$

The stopping power is an essential parameter for calculating the concentration of F and will be estimated using empirical equations and Bragg's law, which states that the stopping cross-section of a compound is given by the weighted average of the effective cross-sections of its constituent elements [54].

4.2.4 Physical principles of the PIGE spectroscopy

In the PIGE technique, the nuclear resonance reactions already described are used to analyze a sample quantitatively and qualitatively. The nuclear energy levels are specific to each isotope, so detecting the specific energy of the gamma rays emitted makes it possible to identify the element [54], [59].

The energy of the bombardment beam, Eb, must be greater than the resonance energy of the nucleus, Er, for studies at depth, or equal for studies on the surface of the sample. The radiation emitted as a result of the incidence of particles with this bombardment energy reflects the concentration of an element in the region at depth where the incident particles are stopped, since the radiation is emitted at the point where the bombardment energy equals the resonance energy of the nucleus (figure 4.3). By measuring the intensity of the gamma radiation emitted as a function of the bombardment energy, sufficient information is obtained to calculate the concentration of an isotope in the sample under study [49].

The technique is restricted to the analysis of light elements, typically between Lithium (Z=3) and calcium (Z=20) where nuclear interactions are more prominent and the influence of the Coulomb force is less, because as the atomic number increases, the intensity of the repulsive Coulomb force of the nucleus increases, making it difficult for the proton beam to interact with the nucleus and the subsequent excitation of protons or neutrons inside the nucleus [49].

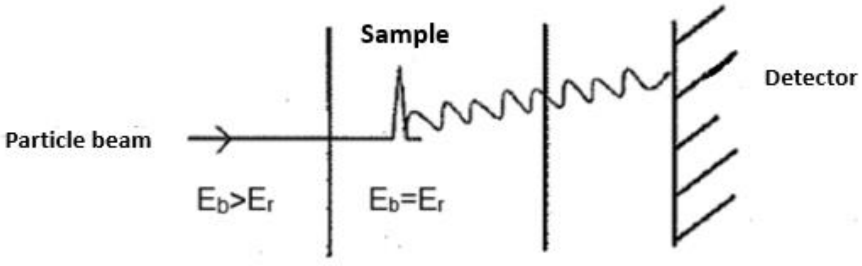

Figure 4.3- Bombardment of the sample with particles with an energy higher than the resonance energy promotes the emission ofγ radiation when the energy of the projectile coincides with the resonance energy of the target (E_b- bombardment energy and E_r- resonance energy). Adapted from [49].

4.3 Advantages and limitations of the techniques

Table 4.2- Advantages and limitations of the Raman and PIGE spectroscopy techniques.

	Advantages	**Limitations**
Raman	Non-destructive technique, fast and non-invasive.	Low signal intensity and fluorescent interference.
	Highly sensitive to the vibrational modes under study.	Dependence on the molecular orientation of the sample.
	Good spatial resolution (up to 1 μm in diameter).	Requires compound concentration greater than 1-5% in the sample.
PIGE	Allows detection of several elements simultaneously, and in-depth analysis.	Requires prior knowledge of the resonance energies of each isotope.
	Good beam resolution (in the order of 0.05 to 1 keV).	Interference from secondary reactions in the matrix and from nearby resonances.
	Non-destructive technique suitable for low Z elements.	Limited to low Z elements.

5

MATERIALS AND METHODS

This chapter describes the materials and methods used to carry out the study, as well as the experimental procedure for preparing the tooth specimens.

5.1 Materials and Methods

The study used a total of 54 human teeth enamel samples, divided into two groups. The control group (C) consisted of 27 samples and the test group (T) also consisted of 27 samples.

The fluoride product used in the study was Duraphat® from the Colgate® brand, consists of sodium fluoride (NaF), where 1 ml of the product contains 50 mg of sodium fluoride, equivalent to 22.6 mg of fluoride, it was acquired from Colgate Palmolive, Unipessoal, Lda.

5.1.1 Sample preparation

The samples used in the study came from healthy teeth extracted for periodontal or orthodontic reasons and stored in the FMDUL GIBBO-LIBPhys tooth bank in a 0.5% chloramine solution at 4 $°C$. To select the samples, a detailed analysis of each tooth specimen was carried out using a binocular magnifying glass (Meiji Techno EMZ 8RT, Japan), to exclude specimens with irregularities in the enamel or decayed teeth.

Molar and premolar teeth were selected and cut using a precision blade (Buehler IsoMET 1000, USA), with a rotation frequency of 525 rpm. The occlusal and root surfaces of the teeth were removed to obtain samples with about 5 mm thick. The faces were cut so that each sample was approximately 5 x 4 mm and 2 mm thick (figure 5.1). The selected samples were divided into pairs, i.e., each tooth provided a pair of samples, one sample for the control and the other for testing.

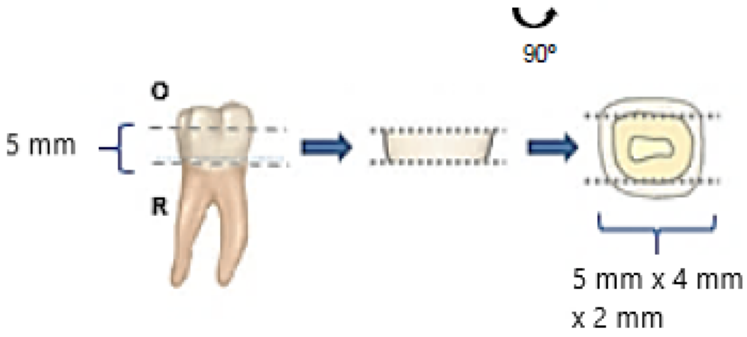

Figure 5.1- Cuts made in the teeth to obtain the samples. Adapted from [49].

5.1.2 Duraphat® application protocol

Duraphat® is recommended for the treatment of dental caries and hypersensitive teeth. It consists of sodium fluoride (NaF), where 1 ml of the product contains 50 mg of sodium fluoride, equivalent to 22.6 mg of fluoride.

Figure 5.2 - Colgate Duraphat®, 50mg/ml sodium fluoride.

Group C

No fluoride-containing product was applied to this group, since the aim of this study was to assess the incorporation of fluoride into the enamel. These samples were used to validate the uptake of fluoride into the enamel by measuring the concentration of F using the PIGE technique. The samples were wrapped in moist absorbent cotton to prevent the enamel from dehydrating.

Group T

For this group, Colgate Duraphat® was applied 3 times over a 12-day period, i.e., every 4 days, lasting 1 minute for each application. After each application, the tooth samples were brushed under running water to remove traces of the product and then wrapped in damp absorbent cotton to prevent dehydration of the enamel at room temperature.

5.1.3 Analysis using PIGE spectroscopy

The experimental work was carried out at the National Accelerator Center (CNA), in Seville, Spain, using a 3.8 MeV proton accelerator.

5.1.3.1 PIGE equipment

The particle accelerator is Pelletron 3 MV Tandem, model 9SDH-2, made by National Electrostatics Corporation (NEC). It uses a high potential gap, up to 3 mega volts (MV), to accelerate protons, alpha particles, and a wide range of ions, figure 5.3.

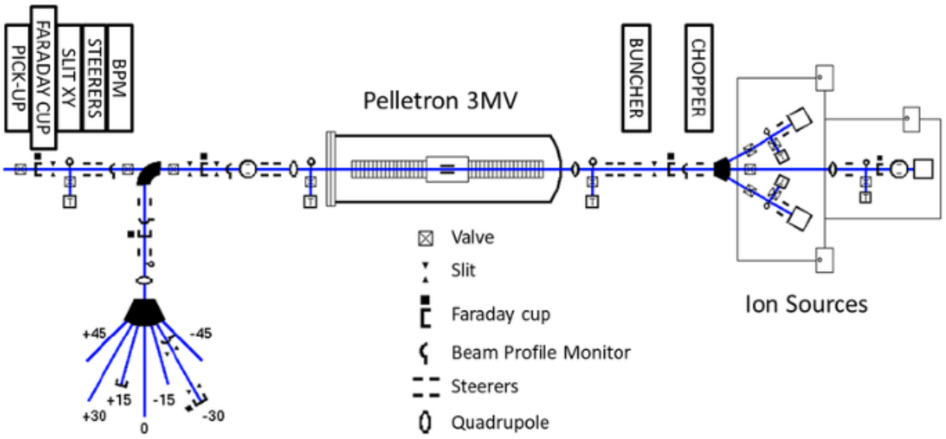

Figure 5.3- Schematic layout of the 3 MV Tandem model 9SDH-2 at CNA [58].

5.1.3.1 Experimental conditions

The experimental work for PIGE was carried out at the CNA, by the 3 MV Tandem accelerator, using 3,8 MeV protons. The current used was approximately 2 nA, and the total charge collected was 0.5, 1 or 1.5 μC per measurement. Before entering the reaction chamber, the beam passes through a collimator which defines a beam spot of around 0.5 mm on the sample, allowing, in this case, three different spots per mandible to be analyzed. The fluorine gamma-rays from the $^{19}F(p,p'\gamma)^{19}F$ nuclear reactions were detected by a HPGe semiconductor detector. Quantification was performed using a relative analytical method by comparing with certified reference materials (CRM) (Bone Ash - NIST 1400 and Bone Meal– NIST 1486) according to following expression [60].

$$C_{sample} = \frac{Y_{sample}\, S_{sample\,(E_F)}}{Y_{CRM}\, S_{CRM\,(E_F)}} \times C_{CRM} \tag{5.1}$$

where C_{sample} and C_{CRM}, are the element concentrations in sample and CRM, respectively; Y_{sample} and Y_{CRM}, are element gamma-ray yields (net peak areas) for sample and CRM, respectively, normalized to the beam charge of the incident protons (corrected by counting dead time); S_{sample} and S_{CRM}, are stopping powers for proton beam of energy E_F.

To calculate the concentration of fluoride in tooth samples, was used the Matlab software to perform the spectra deconvolution, starting by removing the background of the spectrum, then identifying the line in channel 245 of the spectrum, which corresponds to nuclear reaction of interest ($^{19}F(p,p'\gamma)^{19}F$), figure 5.4. Then, the peak intensity (net peak area), was calculated using the Matlab function trapz (Trapezoidal numerical integration), that computes the approximate integral via the trapezoidal method [61], and then construct the regression model using the Matlab function polyfit to fit the data with a first order polynomial [62].

Since the concentration of Bone Ash -NIST 1400 [63], and Bone Meal -NIST 1486 [64], are known, these concentration values were used to construct the calibration curve, a graph of concentration as a function of peak intensity.

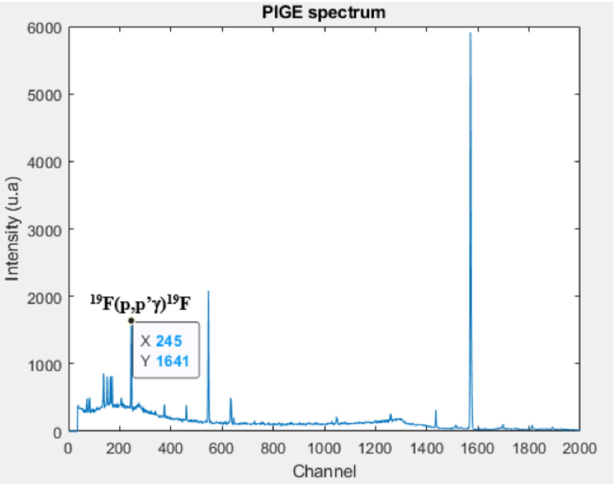

Figure 5.4- PIGE spectra of fluorine gamma-rays from the ^{19}F(p,p'γ)^{19}F nuclear reaction.

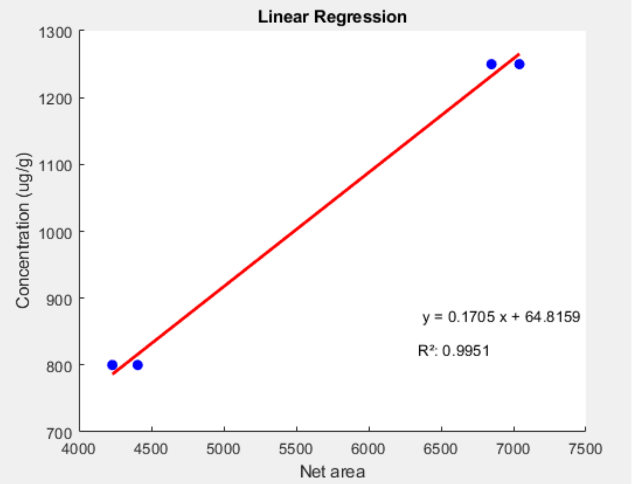

Figure 5.5- Calibration line to calculate fluoride concentration.

The calibration curve equation of the figure 5.5 is the following:

$$y = 0.1705\,x + 64.8159 \tag{5.2}$$

The R-squared (R^2 coefficient of determination) is 0.995, which represent a good data fit of the regression model. The confidence interval for the slop is 0.1705 ± 0.0001 and for the intercept is $65 \pm 2 * 10^2$.

5.1.4 Analysis using Raman spectroscopy

The experimental work was carried out at LIBPhys-UNL, FCT, using XploRA confocal spectrometer.

5.1.4.1 Acquisition of Raman spectra

The XploRA confocal spectrometer (Horiba/Jobin-Yvon Xplora, France) was used, coupled to an Olympus microscope with 10x, 50x and 100x objectives. Each sample was analyzed with a 10x objective, to choose the region of interest to be studied, and in each tooth sample ten different regions were analyzed with the aim of studying the absorption of fluoride by tooth enamel in the most uniform way possible.

To acquire the Raman spectra, a diode laser with a wavelength of 785 nm was used, with a 50% filter, 500 μm hole, 200 μm slit, and a grating of 1200 $grooves/mm$. The spectra were acquired in the region of interest defined between 250 cm^{-1} and 2150 cm^{-1}, each acquisition lasted 15 seconds with 3 repetitions for the same spectrum, with the final spectrum being the average of the 3 repetitions to minimize noise in the spectra.

5.1.4.2 Polarized Raman spectroscopy

The depolarization ratio (DR) is defined according to the relative position between the two collimators: the linear polarizer and the analyzing polarizer. By changing the angle between the collimators to 0° or 90°, it is possible to obtain Raman radiation polarized parallel (||) or perpendicularly (⊥) in relation to the polarization state of the incident beam, respectively. Showed in the annexes 9.7 and 9.8 [65].

To compute the DR, two spectra were acquired for each point under study, one with perpendicular polarization and the other with parallel polarization relative to the polarization of the excitation laser radiation, thus obtaining a set of data representative of the demineralization state of the sample and the effect of fluoride.

5.1.4.3 Preprocessing of Raman spectra

Raman scattering is a weak process, which often results in low signal to noise ratios. Reducing experimental noise, is generally done in three separate steps: (1) cosmic ray removal, (2) signal smoothing, and (3) baseline subtraction [66], [67]. Since the cosmic ray removal is done by the integrated software LabSpec (Horiba/ Jobin-Yvon Xplora, France), the other steps were done on Matlab software.

Two different ways of Raman spectra smoothing was compared: Savitzky–Golay second order filter with a frame length of 25 and moving mean with a sliding window length of 25 was applied to the average of ten spectrum from each sample, using the Matlab function sgolayfilt and movmean [68], [69]. But comparing their performances through the mean squared error (MSE), Savitzky_Golay filter gives better results. After this, the baseline was subtracter from the signal to minimize the effect of a varying background caused by fluorescence of the sample or thermal fluctuations on the device, using the Matlab function detrend [70], which removes the best straight-fit line from the data.

Each spectrum was normalized by its maximum value to ensure that the outcome of the analysis is independent of different Raman scattering collection geometries, since this is important for a quantitative comparison of Raman spectra because of variation on the laser intensity. The peaks of each spectrum were identified using Matlab function findpeaks [71], with a MinPeakWidth of 0.5, a MinPeakHeight of 0.1, and a MinPeakProminence of 0.01. After identifying the interest regions, each peak was fitted to a Gaussian function, using the Matlab function fit [72], with the fit type gauss1, that gives coefficients with 95% confidence bounds, according to the following expression:

$$f(x) = a_1 * \exp\left[-\left(\frac{x - b_1}{c_1}\right)^2\right] \tag{5.3}$$

where a_1 is the amplitude, b_1 is the centroid (location), c_1 is related to the peak width [72].

The preprocessing of the Raman spectra was essential to ensure the reliability of the results, and to ensure that the features extracted from the Raman spectra are reliable and will provide valuable information about the symmetry, crystallinity and the chemical composition of the samples, to be used in ML to classify and predict the concentration of fluoride on the samples.

Features extraction:

- **Centroid of the Raman spectra's peaks**: Is related to the movements of atoms in a molecule. According to the literature, the vibrational mode ν_1 of PO_4^{3-} for the HAp is approximately $959\ cm^{-1}$ and for the FAp there is a shift of approximately $5\ cm^{-1}$ to the higher wavenumbers [13], and this feature is very important in this study, because by comparing the Raman spectra of the C and T samples is expected to have a shift on this peak.
- **Full width at half maximum (FWHM) of the peaks:** Is a measure of the width of the distribution of observed Raman frequencies. It is related to the crystallinity of tooth mineral and is estimated as the reciprocal of the FWHM of $\nu_1\ PO_4^{3-}$ peak. The FWHM was computed using the following expression $2\sqrt{\ln(2)} * c_1$.
- **Intensity of the peaks:** Is related to the amplitude of the Raman scattering process associated with each vibrational mode and can provide information about the crystal structure of the material and was calculated using the function trapz.
- **Depolarization Ratio of $\boldsymbol{\nu_1\ PO_4^{3-}}$:** provides valuable information about the crystal symmetry and orientation of vibrational modes.

5.1.5 Principal Component Analysis (PCA)

Raman spectroscopy generates a large multivariate dataset that consists of a series of data points representing the intensity of Raman scattering at specific frequencies.

PCA is a statistical method used to reduce the dimensionality of a very large dataset while preserving the most relevant information in the data, transforming a set of correlated data into a smaller set of uncorrelated data that maximizes the variance of the system, i.e., preserving as much variability as possible – the main components of the system. The goal is to find new variables that are linear functions of the initial variables, that maximize the variability between them and that are not correlated with each other. PCA also aims to eliminate some of the variables that characterize the system, but which have little weight or little statistical information [73], [74].

PCA start by finding the direction with the greatest statistical information and greatest variability, which is defined as the first principal component. Then, the second principal component will be the one with the lowest variance in relation to the first, but always respecting the condition that it is orthogonal to it. And thus, the various main components of the data set under study are found. With this, two-dimensional graphics are obtained, allowing the visualization of different categories grouped according to their similarity or difference.

PCA was performed in Matlab, using the complete Raman spectra with the aim of identifying the most relevant wavenumbers in the spectra to later be used in classification model. PCA was also performed using the features to extract relevant information and identify patterns in Raman data.

5.1.6 Machine Learning (ML)

With the advancement of artificial intelligence (AI) in recent years, ML has become an effective tool in analytical sciences, and it can be utilized to automatically process and analyze complex Raman spectra. These algorithms can identify and classify different molecular species, phases, or materials present in a sample based on the spectral data [42]. All the study about classification and regression models was programmed on python language using Spyder from the Anaconda Prompt.

5.1.6.1 Classification models

To choose the best ML models for this study, Orange® software was used to visualize and analyze the data and choose the best models with high accuracy for the data classification.

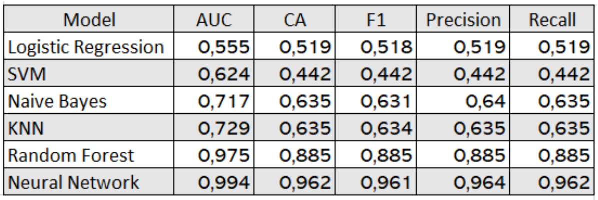

Model	AUC	CA	F1	Precision	Recall
Logistic Regression	0,555	0,519	0,518	0,519	0,519
SVM	0,624	0,442	0,442	0,442	0,442
Naive Bayes	0,717	0,635	0,631	0,64	0,635
KNN	0,729	0,635	0,634	0,635	0,635
Random Forest	0,975	0,885	0,885	0,885	0,885
Neural Network	0,994	0,962	0,961	0,964	0,962

Figure 5.6- Models scores for features extracted from Raman spectra.

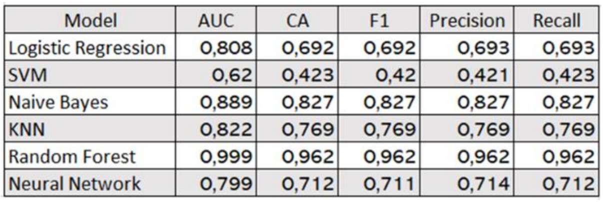

Model	AUC	CA	F1	Precision	Recall
Logistic Regression	0,808	0,692	0,692	0,693	0,693
SVM	0,62	0,423	0,42	0,421	0,423
Naive Bayes	0,889	0,827	0,827	0,827	0,827
KNN	0,822	0,769	0,769	0,769	0,769
Random Forest	0,999	0,962	0,962	0,962	0,962
Neural Network	0,799	0,712	0,711	0,714	0,712

Figure 5.7- Models scores for full Raman spectra.

The samples C_{17} and T_{17} were removed from the original dataset because the concentration of fluoride on the C_{17} samples is greater than the concentration on the T_{17}. After this, the dataset was divided on training (85% of the data) and tests (15% of the data) dataset using the python function train_test_split imported from sklearn.model_selection, where the data was stratified to balance the classes [75], and the data were normalized using the function preprocessing.MinMaxScaler imported from sklearn [76]. The ML models were imported from scikit-learn library in python.

5.1.6.1.1 Random Forest classifier (RF)

Random forest is a meta estimator that fits several decision tree classifiers on various sub-samples of the dataset and uses averaging to improve the predictive accuracy and control overfitting, as it randomly samples data with replacement, selects features, and ranks the features importance by order of nodes, thus improving the resistance of the algorithm to interference [40], [77].

The parameters used to control the model were (n_estimators = 30, criterion='gini', min_samples_split = 4, and bootstrap= True) for both features and Raman spectra and max_samples = 10 for Raman spectra. Then the features importance was calculated to compare with the features extracted and assess whether they are correlated.

5.1.6.1.2 Logistic Regression (LR)

Logistic Regression is a statistical method used to analyze dataset with independent variables that can be used for binary classification problems. The goal in LR is to find the best fitting model by estimating the weights that maximize the likelihood of the observed data given the model and is normally done using optimization algorithms like Conjugate Gradient or gradient descent.

The parameters used to regularize the model were: norm penalty Lasso ('l1'), tolerance for stopping criteria of 0.01, inverse of regularization strength of 15 and maximum number of iterations of 100.

The coefficients associated with each feature were calculated to assess its importance and understanding the influence of the features on the prediction of the target variable. Where larger absolute values imply a stronger influence on the predicted outcome.

5.1.6.2 Regression model

Some regression models were evaluated in this study like Gradient Boosting Regressor (GBR), Support Vector Regression (SVR) and Random Forest Regressor (RFR), to search for the best results, to estimate the enamel fluoride concentration trough the Raman spectra, but the results were not the expected, since only RFR gives R-squared of 0.33 which is far from 1, that it is far from being a reliable regression.

5.1.6.2.1 Random Forest Regressor

Random Forest Regressor is an extension of the Random Forest algorithm, it builds a multitude of decision trees at training time and outputs the mean prediction (regression) of the individual trees.

The parameter selected for the model were, max estimators of 50, max depth of 6 and max features auto. To evaluate the performance of the model MSE and R^2 were calculated.

5.2 Flowchart of the methodology employed in the study

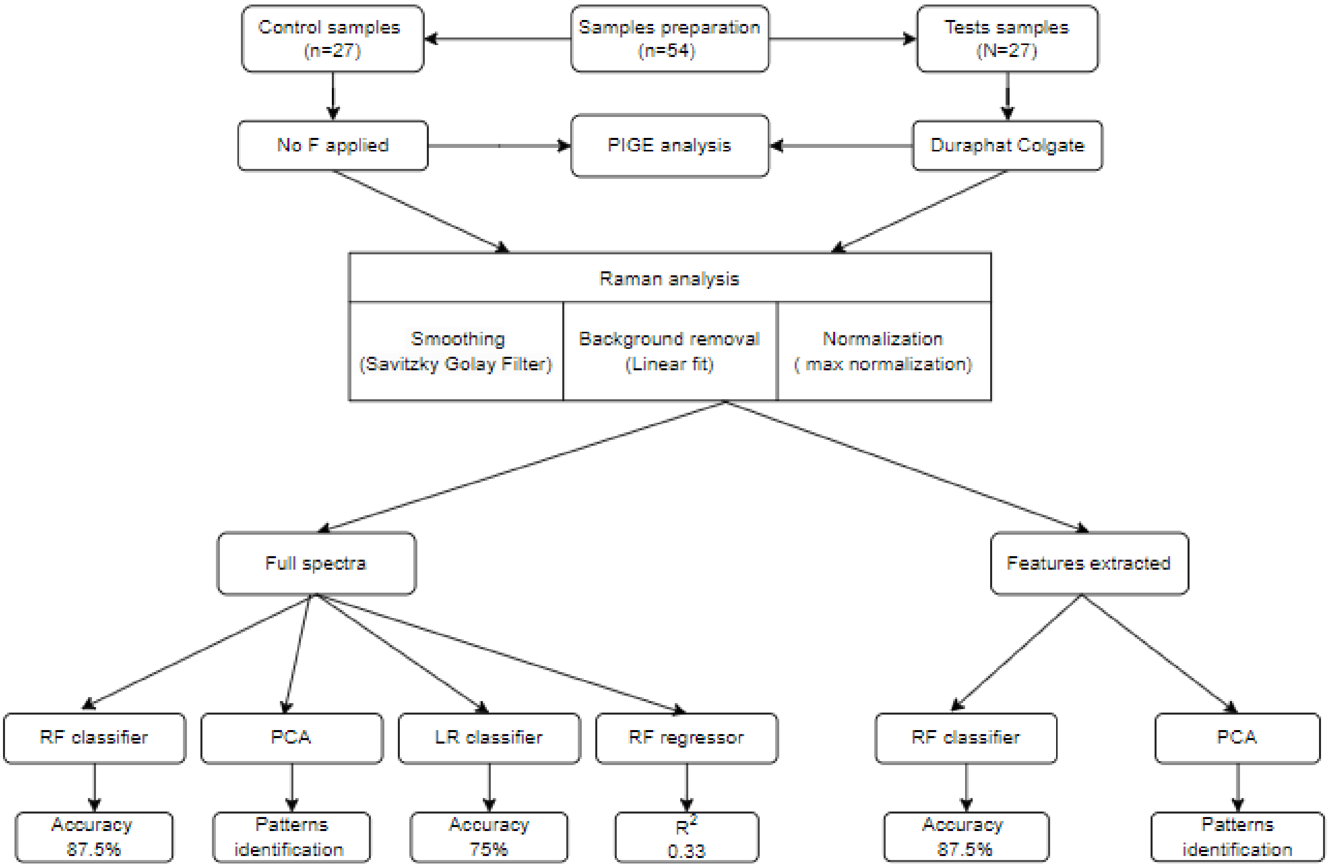

6

RESULTS AND DISCUSSION

In this chapter, the experimental results obtained are presented and discussed. It starts by evaluating the fluorine uptake on tooth enamel, by analyzing the results obtained by PIGE. Then the results obtained by Raman spectra were analyzed, to see if the shift suggested by the literature in the vibrational mode ν_1 of PO_4^{3-} in Raman spectrums was observed. After confirming the shift between samples C and T, the features and full Raman spectrums were analyzed using PCA to reduce de dimensionality and identify patterns. It the end, the dataset was used on ML to estimate the concentration of fluorine and classify the samples on HAp and FAp.

6.1 Results from PIGE study

Fluoride concentrations on the samples were calculated using equation 5.2, where the concentration of fluoride in the reference samples (bone ash and bone meal) were compared with the calculated fluoride concentrations for this samples to evaluate the accuracy of the calibration curve in table 6.1. Then the fluoride concentration on the tooth enamel was calculated for the C and T samples.

Table 6.1- Comparison between reference and calculated concentration values.

	NIST concentration ($\mu g/g$)	Calculated concentration ($\mu g/g$)
Bone Ash	1250	$(12 \pm 2) \times 10^2$
Bone Meal	800	$(8 \pm 2) \times 10^2$

The calculated concentration from the calibration line with their standard uncertainty are in concordance with the reference concentration from NIST, since they are in the confidence interval, which shows a good calibration curve to determine the concentration of fluoride on the samples.

The results obtained for fluoride concentrations in the C and T samples with the respective uncertainty (standard deviation) are presented on figure 6.1.

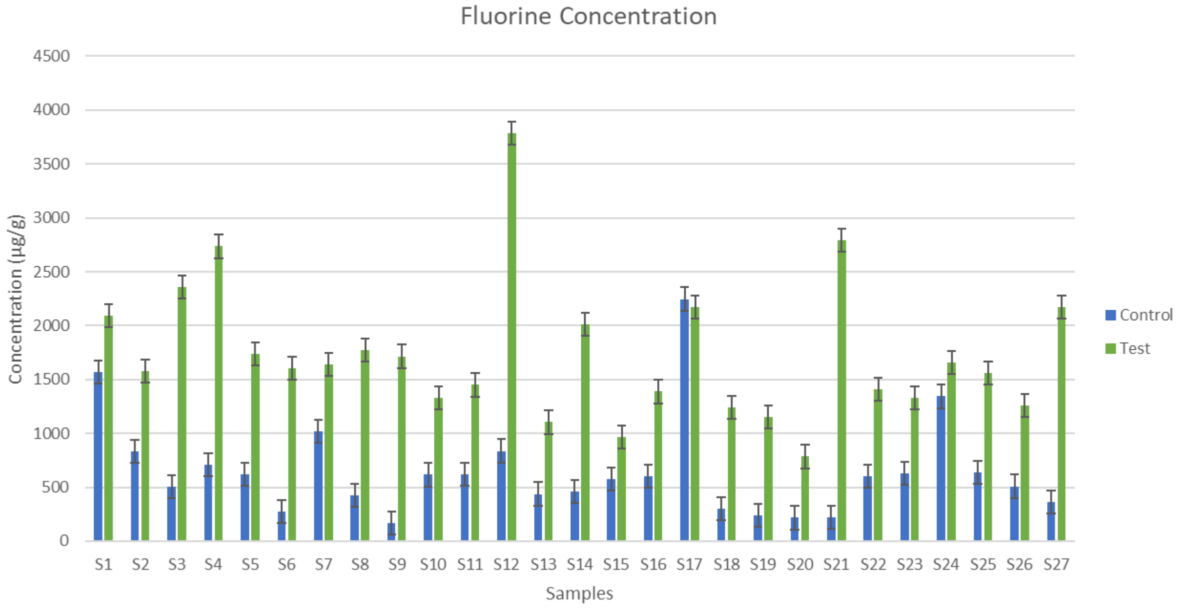

Figure 6.1 - Concentration of fluorine in controls samples in blue and tests samples in green.

In almost all test samples an increase in fluoride concentration was observed when compared with the control sample in each pair, which proves the uptake of fluoride in tooth enamel as suggested by many studies reported in the literature review chapter. For the pair S_{17}, an exception was observed in relation to the other samples, where the concentration of fluoride in the control sample is relatively higher than that in the test, which in principle shows that it is a tooth extracted from an individual exposed to fluoridated products or also represents a decayed tooth, however, was removed from the study.

It is observed that F concentrations in control teeth show quite significant variations, which would be expected since they are extracted from different individuals. The concentration of F varies according to eating habits, age, region of residence and exposure to fluoridated products [6], [78]. On the tests samples there are samples that the uptake of fluorine is higher, and this is related to the ability of the enamel on repair itself, since there is a threshold at which above that the enamel can’t repair, so is expected some change in fluoride concentration between the test samples.

In general, there was an increase average of 160% in the concentration of fluoride in the test samples when compared to the control samples, so, the results obtained from PIGE were quite promising, to observe variations in the Raman spectra between the control and test samples.

6.2 Results from Raman spectroscopy study

The preprocessing of the Raman spectra shows to be important as it improves the interpretation of the spectra and facilitates the analysis of regions of interest. The results are showed in the figure 6.2.

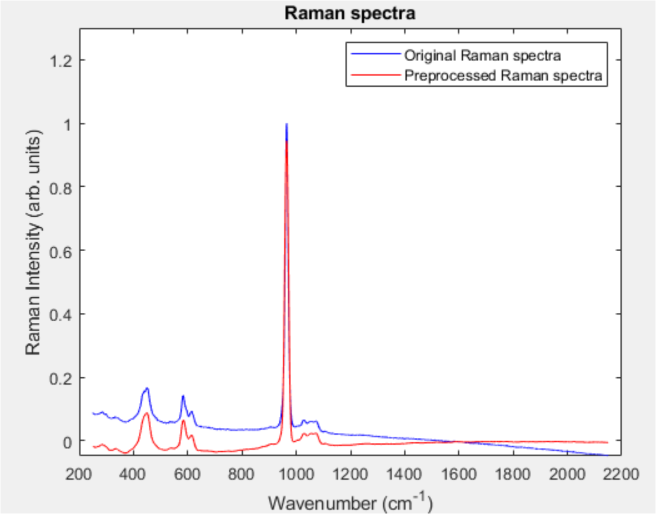

Figure 6.2- Original Raman spectrum (Blue line) and Raman smoothed spectrum, normalized and with baseline correction (Red line).

To visualize difference between Raman spectra of C and T samples, the samples pairs were plot in 2D graphic, an example is showed on figure 6.3 and 6.4.

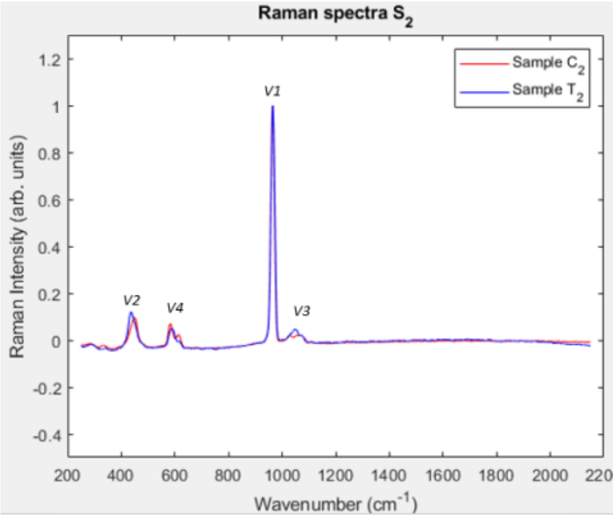

Figure 6.3 Comparison of the Raman spectra between sample C_2 and T_2.

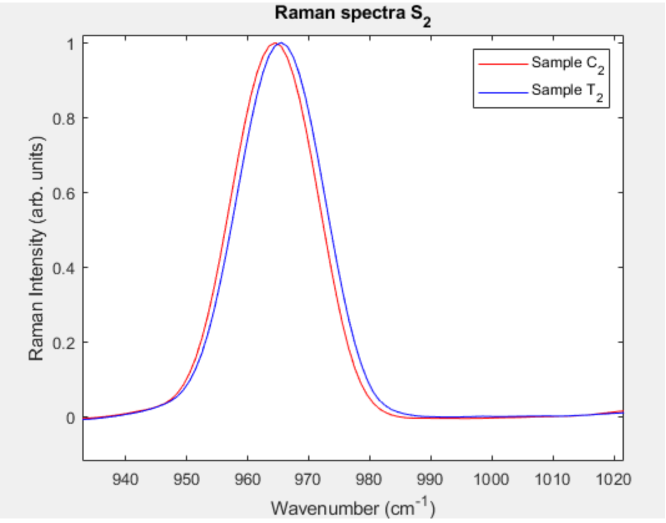

Figure 6.4 -Zoom in Raman spectra in the region of the ν_1 vibration.

There is a shift in the region of the $\nu_1$vibration of the PO_4^{3-} in Raman spectra between HAp and FAp as suggested by literature and Campillo et al. 2010 [13]. The shift depends on the degree of F substitution on the HAp matrix, mainly due to the poor spectral resolution of the Raman microscope. But from figure 6.3 is possible to see some differences in others vibrational modes of PO_4^{3-}, especially on ν_2 and ν_4 vibrations that are normally attributed to changes in the crystal lattice structure and bond strengths and changes on ν_3 is associated with the vibrational modes of fluoride ions at approximately $1030-1100\ cm^{-1}$ [79].

From the figure 6.1, there are some tests samples which the fluorine uptake is bigger than others, and this difference are observed too in the Raman spectra, mainly in $\nu_1$vibration. So, this results shows that using Raman spectra is possible to have an idea about the fluoride concentration on the enamel tooth, and due to the greater difficulty of accessing facilities with particle accelerators (protons) to measure the fluorine concentration, Raman spectroscopy would be an excellent solution if it were possible to calculate the concentration only through Raman spectra.

In summary, the average value of the ν_1 vibration for the control samples was 964.7 ± 0.4 and for the tests it was 964.8 ± 0.3. The shift for higher wavenumber in ν_1 peak is confirmed by the average value, but the difference is still small, which also confirms the need for an effective method to measure the band change since any change in the measurements or small unwanted external interferences can lead to incorrect values.

6.2.1 Depolarization ratio (DR)

DR can be affected by many factors such as mineralization, chemical composition, structural changes, caries lesions, aging. Fluorine uptake in the enamel, change the chemical composition and affect its mineral density, and consequently the depolarization ratio.

The results obtained and its uncertainty (standard deviation) for the depolarization ratio are represented in figure 6.5.

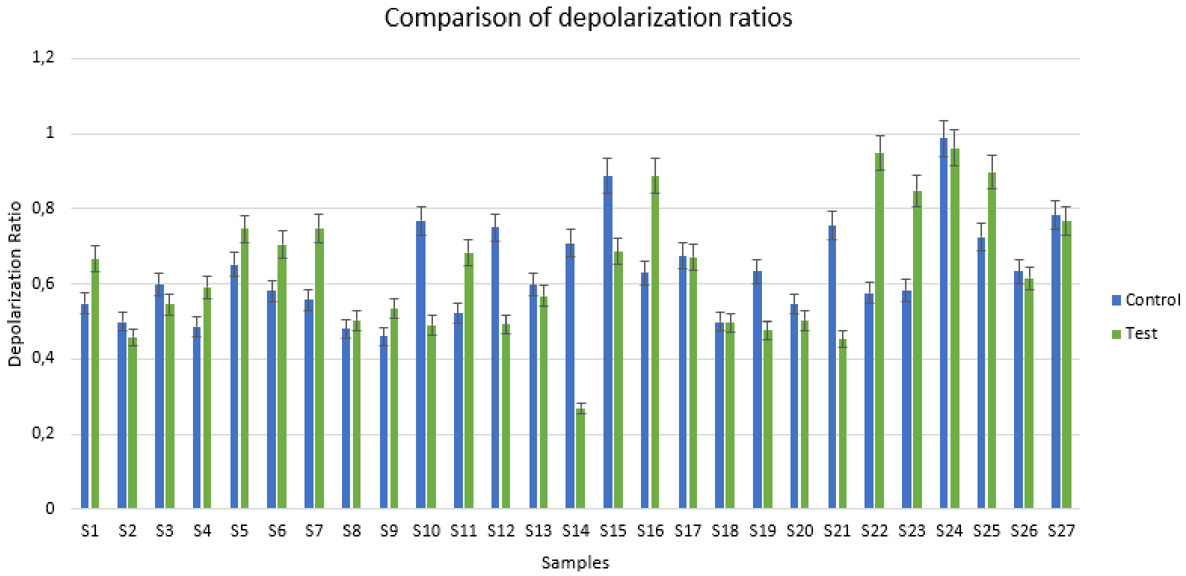

Figure 6.5- Depolarization ratio of the control samples in blue and tests samples in green.

In most of the samples there are small changes on the depolarization ratio, which is related with many factors, so to be more precise, to facilitate the analysis and the understanding of these values, the comparison is made in pairs, that is, only between the two samples of each pair.

In the test's samples, where the fluorine uptake was low, the depolarization ratio varied less than the others, because the chemical composition was less affected. However in some samples like S_{12}, S_{14} and S_{21} where the fluoride uptake was bigger, the depolarization ratio of the tests samples were smaller than their corresponding pair control, and this result show the protective effect of fluoride on enamel when its concentration reaches significant levels, i.e., when there is a change from HAp to FAp in the enamel.

6.3 Results obtained from PCA analysis

It began by analyzing through PCA whether it was possible to identify patterns in the data obtained through Raman spectroscopy. The results using the extracted features are showed on figure 6.6 and 6.7.

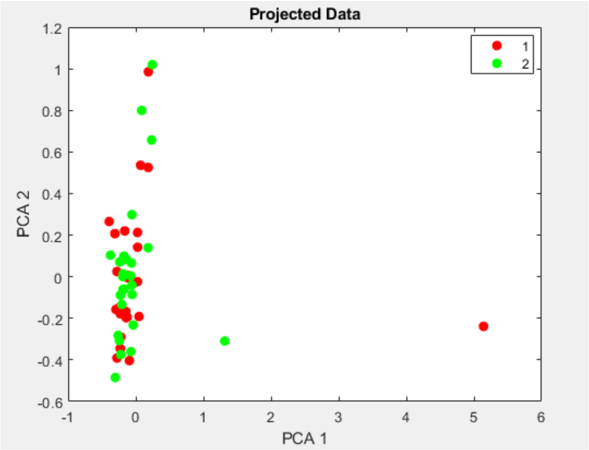

Figure 6.6- PCA of the features extracted from control and tests samples.

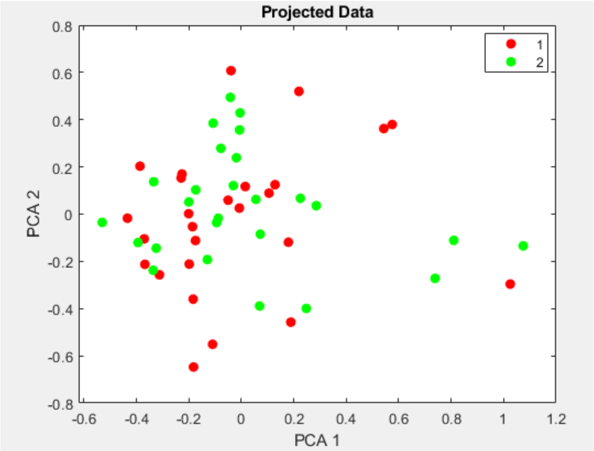

Figure 6.7- PCA of the features extracted from control and tests samples without samples C_{17} and T_{17}.

The samples were separated in 2 groups, i.e., in C on red color and in T on green color, using the features for PCA. On figure 6.6 there are two samples that show a different behavior, and it correspond to the samples C_{17} and T_{17}, so this agrees with the PIGE results, in which the samples have almost the same F concentration. After removing this samples, the data are more spread out on 2D plot and now is possible to identify small groups made up of 4 or 5 samples, associated to the different F concentration.

For the full Raman spectrums, the PCA results are showed on figure 6.8 and 6.9.

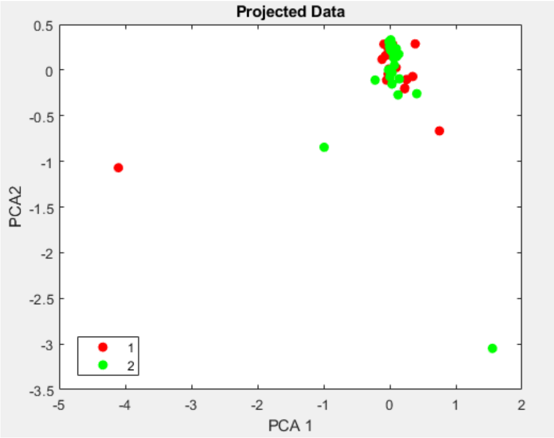

Figure 6.8- PCA of the full Raman spectrum.

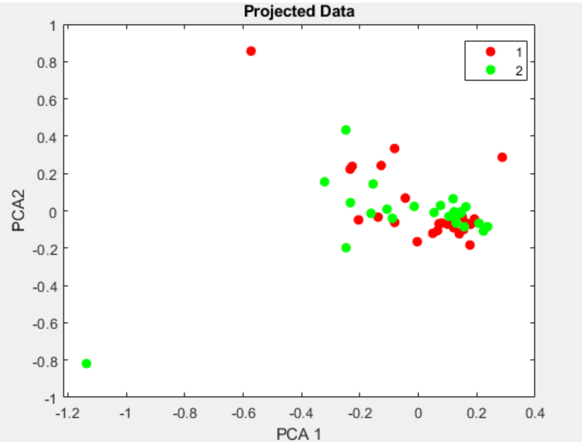

Figure 6.9- Figure 6.9- PCA of the full Raman spectrum without samples C_{17} and T_{17}.

In the figure 6.8 there is a region where the control and tests are completely overlapped, but from the figure 6.9 is possible to see that some samples are more spread out, that is related to the concentration of fluoride, where some control samples have almost same concentration as the tests samples and this samples would be closer, but also is possible to identifying some small groups.

In general, it was not possible using PCA to group the samples into test (FAp) and control (HAp) sets, but it was still possible to identify some patterns when sample S_{17} was removed.

6.4 Results obtained from the application of Machine Learning tools

The ML models for classifier (RF and LR) produced good results with a test accuracy equal or greater than 75%. But for the regression model RFR the results were below expectations, with R^2 about 0.33 and MSE about 0.14.

6.4.1 Results obtained from Random Forest Classifier

The results obtained for the features extracted and for the full Raman spectrums, using 85% of de dataset for training the models were almost the same, where the accuracy in test was for both about 87.5%. The predicted classes with their confusion matrix (columns are the predicted class and rows are the real class) and classification reports are showed on figure 6.10 and 6.11.

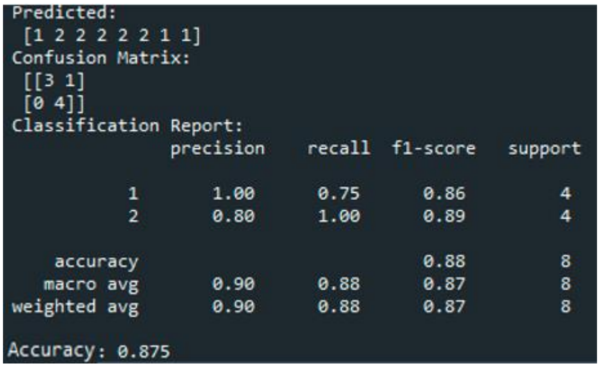

```
Predicted:
 [1 2 2 2 2 2 1 1]
Confusion Matrix:
 [[3 1]
 [0 4]]
Classification Report:
              precision    recall  f1-score   support

           1       1.00      0.75      0.86         4
           2       0.80      1.00      0.89         4

    accuracy                           0.88         8
   macro avg       0.90      0.88      0.87         8
weighted avg       0.90      0.88      0.87         8

Accuracy: 0.875
```

Figure 6.10- Detailed summary of RF classifier results for the features extracted.

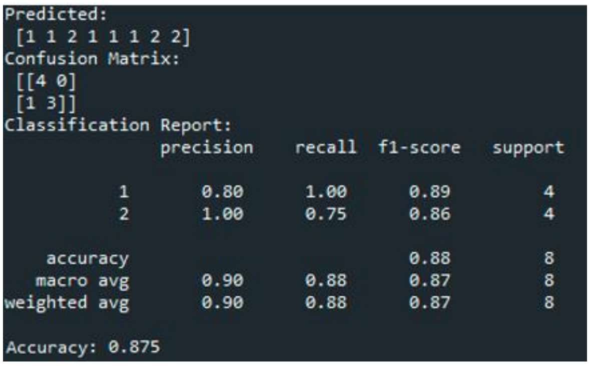

```
Predicted:
 [1 1 2 1 1 1 2 2]
Confusion Matrix:
 [[4 0]
 [1 3]]
Classification Report:
              precision    recall  f1-score   support

           1       0.80      1.00      0.89         4
           2       1.00      0.75      0.86         4

    accuracy                           0.88         8
   macro avg       0.90      0.88      0.87         8
weighted avg       0.90      0.88      0.87         8

Accuracy: 0.875
```

Figure 6.11- Detailed summary of RF classifier results for the full Raman spectrums.

The results for the two different datasets showed that is possible to use data from Raman spectra to classify the C and T spectra, and this study in particular, the sample set is still below a set with significant data variability since it is a set small made up of 52 samples. An accuracy in test of 87.5% is a very good result and opens a window of opportunity to automatically classify Raman spectra. In this study the numbers 1 and 2 represents control and test samples. For both models there is only one sample misclassified, in figure 6.10, one sample of the class 1 was classified as class 2, and in figure 6.11, one sample of the class 2 was classified as class 1, so with a larger dataset the results would even be better.

6.4.2 Results obtained from the Logistic Regression classifier

For this model only the full Raman spectra was used for training and tests, because as suggested by Orange® software this classifier model would not produce good results for the extracted features. The figure 6.12 show the summarized results of the model.

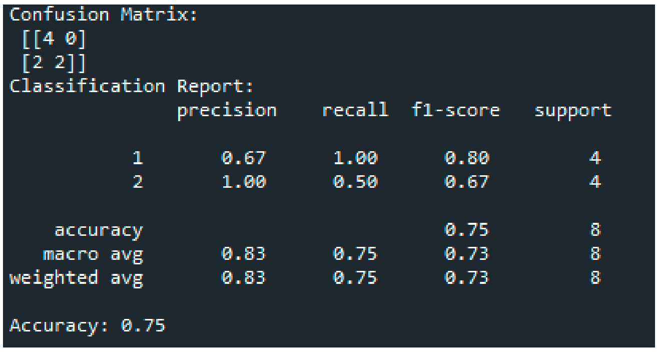

```
Confusion Matrix:
 [[4 0]
 [2 2]]
Classification Report:
               precision    recall  f1-score   support

           1       0.67      1.00      0.80         4
           2       1.00      0.50      0.67         4

    accuracy                           0.75         8
   macro avg       0.83      0.75      0.73         8
weighted avg       0.83      0.75      0.73         8

Accuracy: 0.75
```

Figure 6.12- Detailed summary of LR classifier results.

The accuracy in test is about 75%, below the desired value, and there are two samples misclassified. In futures studies the results of the classifier can be improved using a large and most diversified dataset of data.

6.4.3 Results from Random Forest Regressor

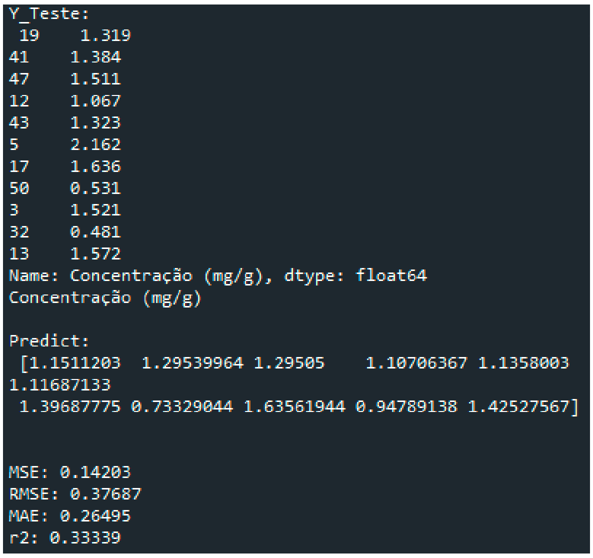

```
Y_Teste:
 19    1.319
41    1.384
47    1.511
12    1.067
43    1.323
5     2.162
17    1.636
50    0.531
3     1.521
32    0.481
13    1.572
Name: Concentração (mg/g), dtype: float64
Concentração (mg/g)

Predict:
 [1.1511203  1.29539964 1.29505    1.10706367 1.1358003
1.11687133
 1.39687775 0.73329044 1.63561944 0.94789138 1.42527567]


MSE: 0.14203
RMSE: 0.37687
MAE: 0.26495
r2: 0.33339
```

Figure 6.13- Results from the RFR model.

Despite the advantages of achieving a good regression model, due to the great difficulty of having access to proton accelerators to perform the PIGE technique in different samples preparing stages, to measure the concentration of fluoride in human enamel. Figure 6.13 shows the summarized results of the regression model, the results were far below expectations. However to improve the results, we suggested that in each stage, after applying the product containing fluoride, the concentration of fluoride in human enamel should be measure and the Raman spectra of the sample.

In this way, it would continuously evaluate the fluorine uptake into the enamel and its corresponding changes in the Raman spectrums, thus creating greater data variability and larger dataset to build a good regression model.

In general, the study demonstrated that the human enamel can incorporate fluorine in high concentrations and also showed that, in principle, FAp is formed in human tooth enamel, since, through the analysis of Raman spectra, it was observed the shift to higher wavenumber as suggested in several previous studies, in ν_1 vibration of the PO_4^{3-}. Also, showed changes in the depolarization ratio of the ν_1 peak, which is related to changes in the structure and chemical composition of the enamel. However, comparing the average value of the shift it was found that the difference between Control (HAp) and Tests (FAp) samples was around 0.1 cm^{-1}, which is a small value, that only very precise techniques can discriminate, hence the need for this study, to demonstrate that is possible to measure small variations between the two compounds using Raman spectroscopy. In the Raman spectra, CaF_2 compounds was not evidenced, since no significant variations were observed around $322\ cm^{-1}$, associated to the most prominent peak in the crystal lattice of CaF_2 [80]–[83].

The results obtained by ML also showed that it is possible to combine spectroscopic techniques with AI and improve the analysis of spectra, but also gave good indications that different compounds can be classified using ML algorithms. For future studies, it will be very important to combine these techniques to facilitate the process of identifying compounds and may also facilitate the determination of the concentration of different compounds in enamel, if a more accurate regression model is built.

7

CONCLUSIONS AND FUTURE PERSPECTIVES

7.1 Conclusions

In this work was evaluated how fluoride is introduced into the HAp matrix, but also was analyzed the effect of F in the enamel, i.e., the changes that different concentration of fluoride can produce in the enamel, since the chemical composition and the structure of the enamel was altered. The spectroscopic technique PIGE was used to measure the concentration of fluoride in the enamel after samples preparation, and it shows that there was variation in the concentration of fluoride between the control and test samples pair, and among the samples. Raman spectroscopy was also used to study the molecular vibration of the enamel, specifically the vibrational modes of phosphate ions PO_4^{3-} , that are the basic building blocks in the crystal lattice structure of both HAp and FAp, and for this two minerals some changes on the Raman spectra was observed, also changes on the depolarization ratio that is related to the different chemical and structural composition. The dataset generated from this spectroscopic technique was after used in ML to classify the samples as Control or Test sample and to estimate the F samples concentrations.

From PIGE results, in almost all the tests samples the F concentration was greater than the control samples, but there was an exception, where the sample C_{17} had more fluoride than the sample T_{17}, and this samples were excluded for the ML study.

From the Raman spectra, many difference between control and tests samples was observed, mainly in ν_1, ν_3 and ν_4 vibrational modes. A shift to higher wavenumbers in ν_1 vibration was observed, but in some sample's pairs where the difference of F concentration was less than around 70%, the shift was so small, that only a very precise technique could discriminate it. And as suggested by some study this is because the Raman spectrums are affected by the degree of substitution of F on the HAp matrix, concluding that, when the degree of F substitution is close to saturation the shift is greater. But the average shift between the two sample's groups was around 0.1 cm^{-1}, and this can be interpreted as a prove that the shift can be measured by Raman spectroscopy.

The depolarization ratio didn’t show reproducibility, because in some pairs the DR of the control samples was greater than the tests and in others the opposite. However, those samples where the F concentration in tests was greater like S_{12}, S_{14} and S_{21} it shows some reproducibility, and all this test samples had a smaller DR than the corresponding control pair.

It was not possible distinguish between control and test samples using PCA, because the samples were overlapped, but PCA was important to identify some patterns and see the behavior of the samples, and remove the sample S_{17} from the study, which increase the variability of the data.

Random forest classifier shows good results for both classifications, using features extracted and full Raman spectra, with an accuracy in test about 87.5%, which shows that ML can be used to distinguish different chemical compounds using data generated by Raman spectroscopy and produce reliable results. On the other hand, the regression study using RFR didn’t produce good results, where the determination coefficient R^2 is around 0.33 a result far from 1 which represent a good model regression. However, in future's studies is possible to improve this result, where the main goal of the study would be to find a regression model that can fit the data in a properly way and get more information about the concentration in the enamel during the samples preparation.

7.2 Limitations and future perspectives

In this study we tried to overcome most of the limitations by finding solutions for them, however we can't progressively evaluate the raising of the fluoride concentration in the samples, because the PIGE study is carried out in Spain, and this had a very negative impact on the regression model. Others possible limitations are related with the time consumption to have a representative dataset from Raman spectroscopy since it takes time to have the desirable dataset. But also related to the human teeth availability, without serious carious lesions, to still be able to carry out remineralization.

In future studies, would be very important measuring the fluoride concentration and vibrational modes at each stage of sample preparation, because it would allow to have a larger dataset with more information, and would be essential in studying the shift in the ν_1 vibration and comparing it in each stage, but it would also greatly improve ML results.

8

BIBLIOGRAPHIC REFERENCE

[1] M. Sandholzer *et al.*, "Micro-CT analysis of human teeth after exposure to controlled thermal stress." ResearchGate [Online]. Available: https://www.researchgate.net/publication/209233992.

[2] G. Orilisi *et al.*, "New insights from Raman MicroSpectroscopy and Scanning Electron Microscopy on the microstructure and chemical composition of vestibular and lingual surfaces in permanent and deciduous human teeth," *Spectrochim Acta A Mol Biomol Spectrosc*, vol. 260, Nov. 2021, doi: 10.1016/j.saa.2021.119966.

[3] "Organização Mundial de Saúde e a Saúde Oral," *O JornalDentistry*, Mar. 2019, Accessed: Aug. 14, 2023. [Online]. Available: https://www.jornaldentistry.pt/news/noticias/organizacao-mundial-de-saude-e-a-saude-oral

[4] A. Jailani *et al.*, "Trans-Cinnamaldehyde Eluting Porous Silicon Microparticles Mitigate Cariogenic Biofilms," *Pharmaceutics*, vol. 14, no. 7, Jul. 2022, doi: 10.3390/pharmaceutics14071428.

[5] M. Shahmoradi, L. E. Bertassoni, H. M. Elfallah, and M. Swain, "Fundamental Structure and Properties of Enamel, Dentin and Cementum," 2014, pp. 511–547. doi: 10.1007/978-3-642-53980-0_17.

[6] J. E. Martin, D. Vance, and V. Balter, "Magnesium stable isotope ecology using mammal tooth enamel," *Proc Natl Acad Sci U S A*, vol. 112, no. 2, pp. 430–435, Jan. 2015, doi: 10.1073/pnas.1417792112.

[7] L. W. Boushell and J. R. Sturdevant, "Clinical significance of dental anatomy, histology, physiology, and occlusion," in *Sturdevant's Art and Science of Operative Dentistry*, Elsevier, 2018, pp. 1–39. doi: 10.1016/B978-0-323-47833-5.00001-0.

[8] C. Xu, R. Reed, J. P. Gorski, Y. Wang, and M. P. Walker, "The distribution of carbonate in enamel and its correlation with structure and mechanical properties," *J Mater Sci*, vol. 47, no. 23, pp. 8035–8043, Dec. 2012, doi: 10.1007/s10853-012-6693-7.

[9] D. D. Arola, S. Gao, H. Zhang, and R. Masri, "The Tooth: Its Structure and Properties," *Dental Clinics of North America*, vol. 61, no. 4. W.B. Saunders, pp. 651–668, Oct. 01, 2017. doi: 10.1016/j.cden.2017.05.001.

[10] E. Beniash *et al.*, "The hidden structure of human enamel," *Nat Commun*, vol. 10, no. 1, Dec. 2019, doi: 10.1038/s41467-019-12185-7.

[11] T. Kodaka, "Scanning electron microscopic observations of surface prismless enamel formed by minute crystals in some human permanent teeth," 2003.

[12] R. P. Shellis, "A SCANNING ELECTRON-MICROSCOPIC STUDY OF SOLUBILITY VARIATIONS IN HUMAN ENAMEL AND DENTINE," 1996.

[13] M. Campillo, P. D. Lacharmoise, J. S. Reparaz, A. R. Goñi, and M. Valiente, "On the assessment of hydroxyapatite fluoridation by means of Raman scattering," *Journal of Chemical Physics*, vol. 132, no. 24, Jun. 2010, doi: 10.1063/1.3428556.

[14] G. Luís *et al.*, "Evaluation of enamel demineralization and fluorine uptake caused by gustatory stimulants of salivary secretion (GSSS) using Raman spectroscopy and proton induced gamma-ray emission (PIGE)," *Journal of Raman Spectroscopy*, vol. 50, no. 3, pp. 380–386, Mar. 2019, doi: 10.1002/jrs.5532.

[15] Kateline Marisa Dias, Maria Micaela Leal da Fonseca, and Sofia Pessanha, "Determinação da distribuição de flúor em esmalte dentário," *Dissertação para obtenção do Grau de Mestre em Engenharia Biomédica*, 2020.

[16] C. J. Chung, B. H. Wu, J. F. Lin, C. F. Han, S. F. Chuang, and W. L. Li, "Nano-structure and nano-mechanical properties of human teeth," in *NEMS 2011 - 6th IEEE International Conference on Nano/Micro Engineered and Molecular Systems*, 2011, pp. 593–596. doi: 10.1109/NEMS.2011.6017425.

[17] R. A. Harper *et al.*, "Acid-induced demineralisation of human enamel as a function of time and pH observed using X-ray and polarised light imaging," *Acta Biomater*, vol. 120, pp. 240–248, Jan. 2021, doi: 10.1016/j.actbio.2020.04.045.

[18] A. Balic, "Biology explaining tooth repair and regeneration: A mini-review," Gerontology, vol. 64, no. 4. S. Karger AG, pp. 382–388, Jun. 01, 2018. doi: 10.1159/000486592.

[19] A. Warreth, E. Abuhijleh, M. A. Almaghribi, G. Mahwal, and A. Ashawish, "Tooth surface loss: A review of literature," *Saudi Dental Journal*, vol. 32, no. 2. Elsevier B.V., pp. 53–60, Feb. 01, 2020. doi: 10.1016/j.sdentj.2019.09.004.

[20] Y. G. de S. Né *et al.*, "Treatment for dental erosion: a systematic review of in vitro studies," *PeerJ*, vol. 10, p. e13864, Nov. 2022, doi: 10.7717/peerj.13864.

[21] D. Franco *et al.*, "Cárie e erosão dentária: uma breve revisão Dental caries and erosion: a soon review." [Online]. Available: www.cro-pe.org.br

[22] T. Saads Carvalho and A. Lussi, “Chapter 9: Acidic beverages and foods associated with dental erosion and erosive tooth wear,” in *Monographs in Oral Science*, vol. 28, S. Karger AG, 2019, pp. 91–98. doi: 10.1159/000455376.

[23] “Recommend the floss patients will actually want to use,” 1982. [Online]. Available: http://www.gcamerica.com

[24] N. Pechlivani, D. A. Devine, P. D. Marsh, A. Mighell, and S. J. Brookes, “Novel methodology for determining the effect of adsorbates on human enamel acid dissolution,” *Arch Oral Biol*, vol. 85, pp. 46–50, Jan. 2018, doi: 10.1016/j.archoralbio.2017.09.035.

[25] N. R. Mohammed, R. J. M. Lynch, and P. Anderson, “Effects of fluoride concentration on enamel demineralization kinetics in vitro,” *J Dent*, vol. 42, no. 5, pp. 613–618, 2014, doi: 10.1016/j.jdent.2013.12.005.

[26] A. D. Paro, M. Hossain, T. J. Webster, and M. Su, “Monte Carlo and analytic simulations in nanoparticle-enhanced radiation therapy,” *Int J Nanomedicine*, vol. 11, pp. 4735–4741, Sep. 2016, doi: 10.2147/IJN.S107624.

[27] M. Campillo, P. D. Lacharmoise, J. S. Reparaz, A. R. Goñi, and M. Valiente, “On the assessment of hydroxyapatite fluoridation by means of Raman scattering,” *Journal of Chemical Physics*, vol. 132, no. 24, Jun. 2010, doi: 10.1063/1.3428556.

[28] L. Guntermann, A. Rohrbach, E. Schäfer, and T. Dammaschke, “Remineralization and protection from demineralization: effects of a hydroxyapatite-containing, a fluoride-containing and a fluoride- and hydroxyapatite-free toothpaste on human enamel in vitro,” *Head Face Med*, vol. 18, no. 1, Dec. 2022, doi: 10.1186/s13005-022-00330-5.

[29] N. S. Nupur, H. v Nilam, J. S. Suyash, R. B. Naveen, K. Vishal, and A. Professor, “Dental Fluorosis in Children: Review,” *Journal of Pharmaceutical Negative Results ¦*, vol. 13, p. 2022, doi: 10.47750/pnr.2022.13.

[30] G. Rajarajan, R. Pradeep Kumar, and S. Pavithra Priyadorshini, “A review on the ethics of artificial water fluoridation,” 2019.

[31] H. Trendley Dean, “Some Reflections on the Epidemiology of Fluorine and Dental Health,” 1953.

[32] S. Hotel and H. T. Dean, “INTERNATIONAL ASSOCIATION FOR DENTAL RESEARCH PROCEEDINGS OF THE TWENTY-THIRD GENERAL MEETINGI I. REMARKS OF RETIRING PRESIDENT,” 1945.

[33] A. Lubojanski *et al.*, “The Safety of Fluoride Compounds and Their Effect on the Human Body—A Narrative Review,” *Materials*, vol. 16, no. 3. MDPI, Feb. 01, 2023. doi: 10.3390/ma16031242.

[34] Annette Wiegand, and Thomas Attin, “Influence of Fluoride on the Prevention of Erosive Lesions-a Review.” Oral Health Prev Dent 2003.

[35] P. I. H. B. L. K. F. G. and M. A. B. K. H. Akkus, “Fluoride incorporation in human enamel during remineralization - A dynamic secondary ion mass spectrometry and Raman microscopy study,” *J Dent*, vol. 62, pp. 68–73, Aug. 2017.

[36] A. C-T Ko *et al.*, “Detection of early dental caries using polarized Raman spectroscopy "Use of optical coherence tomography for assessment of dental caries: quantitative procedure,” 1999.

[37] H. Komatsu *et al.*, “Fluorine analysis of human enamel around fluoride-containing materials under different pH-cycling by μ-PIGE/PIXE system,” in *Nuclear Instruments and Methods in Physics Research, Section B: Beam Interactions with Materials and Atoms*, Oct. 2011, pp. 2274–2277. doi: 10.1016/j.nimb.2011.02.042.

[38] W. Arshed, O. A. Akanle, and N. M. Spyrou, “THE DISTRIBUTION OF FLUORINE AND OTHER ELEMENTS IN TEETH USING PROTON INDUCED REACTION ANALYSIS TECHNIQUES,” 1994.

[39] “Dias_2020”.

[40] I. Otel *et al.*, “Investigation of the protective suitability of a dental fluorinated varnish by means of X Ray fluorescence and Raman spectroscopy,” *Journal of Trace Elements in Medicine and Biology*, vol. 71, May 2022, doi: 10.1016/j.jtemb.2022.126938.

[41] T. Bocklitz, A. Walter, K. Hartmann, P. Rösch, and J. Popp, “How to pre-process Raman spectra for reliable and stable models,” *Anal Chim Acta*, vol. 704, no. 1–2, pp. 47–56, Oct. 2011, doi: 10.1016/j.aca.2011.06.043.

[42] Y. Qi *et al.*, “Recent Progresses in Machine Learning Assisted Raman Spectroscopy,” *Advanced Optical Materials*. John Wiley and Sons Inc, Jul. 18, 2023. doi: 10.1002/adom.202203104.

[43] J. R. Ferraro, K. Nakamoto, and C. W. Brown, *Introductory Raman spectroscopy*. Academic Press, 2003.

[44] T. W. Hänsch *et al.*, “Confocal Raman Microscopy (Springer Series in Optical Sciences 158),” 2011. [Online]. Available: http://www.springer.com/series/624

[45] R. P. Millen, D. Lúcia, A. De Faria, and M. L. A. Temperini, “MODELOS PARA DISPERSÃO RAMAN EM POLÍMEROS CONJUGADOS,” 2005.

[46] F. A. Shah, “Towards refining Raman spectroscopy-based assessment of bone composition,” *Sci Rep*, vol. 10, no. 1, Dec. 2020, doi: 10.1038/s41598-020-73559-2.

[47] K. D. Litasov and N. M. Podgornykh, “Raman spectroscopy of various phosphate minerals and occurrence of tuite in the Elga IIE iron meteorite,” *Journal of Raman Spectroscopy*, vol. 48, no. 11, pp. 1518–1527, Nov. 2017, doi: 10.1002/jrs.5119.

[48] R. H. Brody, H. G. M. Edwards, and A. M. Pollard, “Chemometric methods applied to the differentiation of Fourier-transform Raman spectra of ivories,” 2001.

[49] S. L. Silva *et al.*, “Efeitos no esmalte dentário de produtos branqueadores contendo flúor," Dissertação para obtenção do Grau de Mestre em Engenharia Biomédica, 2018.

[50] D. G. Carvalho, “ESTUDO DA VIABILIDADE DO USO DA ESPECTROSCOPIA RAMAN PARA DETECÇÃO E MONITORAMENTO DE CAROTENOIDES EM POLPA DE Bunchosia glandulifera,” 2018.

[51] Michael F. L’Annunziata, *Radioactivity Introduction and History, From the Quantum to Quarks*, 2nd ed. Elsevier Science, 2016.

[52] “The PIGE (Particle Induced Gamma-ray Emission).” Accessed: Sep. 10, 2023, [Online]. Available: https://www.cmam.uam.es/wp-content/uploads/2022/02/pige.pdf

[53] M. Chiari and I. N. F. N. Florence, “2495-08 Joint ICTP-IAEA Workshop on Nuclear Data for Analytical Applications Fundamentals of the Particle Induced Gamma-ray Emission (PIGE) technique, experimental procedures and examples of PIGE analysis.”

[54] M. FONSECA, "ANÁLISE DE ELEMENTOS LEVES POR REACÇÕES NUCLEARES COM PRODUÇÃO DE RADIAÇÃO GAMA,” Dissertação para obtenção do Grau de Doutor em Física Nuclear, Universidade NOVA de Lisboa, 2010.

[55] “Development of a Reference Database for Particle Induced Gamma Ray Emission (PIGE) Spectroscopy IAEA TECDOC SERIES,”

[56] S. CARMO, "STUDIES ON LOW-ENERGY PARTICLE-INDUCED SOFT X-RAY EMISSION,” Dissertação para obtenção do Grau de Mestre em Engenharia Física, Universidade de Coimbra, 2010.

[57] P. Dimitriou *et al.*, “Development of a Reference Database for Particle-Induced Gamma-ray Emission spectroscopy,” *Nucl Instrum Methods Phys Res B*, vol. 371, pp. 33–36, Mar. 2016, doi: 10.1016/j.nimb.2015.09.052.

[58] F. Lourenço, “A Reacção Nuclear 23 Na(p,p′γ) 23 Na-Optimização da Linha de PIGE do Acelerador Tandem de 3 MV da UFA-ITN," Dissertação para obtenção do Grau de Mestre em Engenharia Física, Universidade de Coimbra, 2010.

[59] D. J. Muensterman *et al.*, “Disposition of Fluorine on New Firefighter Turnout Gear,” *Environ Sci Technol*, vol. 56, no. 2, pp. 974–983, Jan. 2022, doi: 10.1021/acs.est.1c06322.

[60] J.P. Hirvonen, *Handbook of Modern Ion Beam Material Analysis*. Pittsburgh: Material Research Society, 1995.

[61] "trapz." Accessed: Sep. 14, 2023. [Online]. Available: https://www.mathworks.com/help/matlab/ref/trapz.html

[62] "polyfit." Accessed: Sep. 21, 2023. [Online]. Available: https://www.mathworks.com/help/matlab/ref/polyfit.html

[63] "Standard Reference Material 1400 - TSAPPS at NIST." Accessed: Sep. 19, 2023. [Online]. Available: https://tsapps.nist.gov/srmext/certificates/1400.pdf

[64] "SRM 1486 | Certificate of Analysis - TSAPPS at NIST." Accessed: Sep. 19, 2023. [Online]. Available: https://tsapps.nist.gov/srmext/certificates/1486.pdf

[65] Z. X. L. M.-L. T. P.-H. Liu Xue-Lu, "Different angle-resolved polarization configurations of Raman spectroscopy: A case on the basal and edge plane of two-dimensional materials." Accessed: Sep. 20, 2023. [Online]. Available: https://cpb.iphy.ac.cn/article/2017/1892/cpb_26_6_067802/cpb_26_6_067802_f1.jpg.html

[66] J. Wahl, M. Sjödahl, and K. Ramser, "Single-Step Preprocessing of Raman Spectra Using Convolutional Neural Networks," *Appl Spectrosc*, vol. 74, no. 4, pp. 427–438, Apr. 2020, doi: 10.1177/0003702819888949.

[67] S. J. Barton, T. E. Ward, and B. M. Hennelly, "Algorithm for optimal denoising of Raman spectra," *Analytical Methods*, vol. 10, no. 30, pp. 3759–3769, Aug. 2018, doi: 10.1039/c8ay01089g.

[68] "sgolayfilt." Accessed: Sep. 21, 2023. [Online]. Available: https://www.mathworks.com/help/signal/ref/sgolayfilt.html

[69] "movmean." Accessed: Sep. 21, 2023. [Online]. Available: https://www.mathworks.com/help/matlab/ref/movmean.html

[70] "detrend." Accessed: Sep. 21, 2023. [Online]. Available: https://www.mathworks.com/help/matlab/ref/detrend.html

[71] "Find Peaks in Data." Accessed: Sep. 21, 2023. [Online]. Available: https://www.mathworks.com/help/signal/ug/find-peaks-in-data.html

[72] "Gaussian Models." Accessed: Sep. 21, 2023. [Online]. Available: https://www.mathworks.com/help/curvefit/gaussian.html

[73] S. Wold, K. Esbensen, and P. Geladi, "Principal Component Analysis."

[74] I. T. Jollife and J. Cadima, "Principal component analysis: A review and recent developments," *Philosophical Transactions of the Royal Society A: Mathematical, Physical and*

Engineering Sciences, vol. 374, no. 2065. Royal Society of London, Apr. 13, 2016. doi: 10.1098/rsta.2015.0202.

[75] “sklearn.model_selection.train_test_split.” Accessed: Sep. 22, 2023. [Online]. Available: https://scikit-learn.org/stable/modules/generated/sklearn.model_selection.train_test_split.html

[76] “Preprocessing data.” Accessed: Sep. 22, 2023. [Online]. Available: https://scikit-learn.org/stable/modules/preprocessing.html

[77] “Random Forest Classifier.” Accessed: Sep. 22, 2023. [Online]. Available: https://scikit-learn.org/stable/modules/generated/sklearn.ensemble.RandomForestClassifier.html

[78] M. A. R. Buzalaf, A. C. Magalhães, and A. Wiegand, “Alternatives to Fluoride in the prevention and treatment of dental erosion,” in *Erosive Tooth Wear: From Diagnosis to Therapy*, S. Karger AG, 2012, pp. 244–252. doi: 10.1159/000360557.

[79] D. R. T. Y. H. S. N. Lafuente B, “RRUFF Database.” Accessed: Apr. 01, 2023. [Online]. Available: https://rruff.info/chem=Ca,F/display=default/

[80] Q. Williams and E. Knittle, “INFRARED AND RAMAN SPECTRA OF Ca5(P04)3F2-FLUORAPATITE AT HIGH PRESSURES: COMPRESSION-INDUCED CHANGES IN PHOSPHATE SITE AND DAVYDOV SPLITTINGS,” 1994.

[81] I. Alencar *et al.*, “Irradiation effects in CaF2 probed by Raman scattering,” *Journal of Raman Spectroscopy*, vol. 47, no. 8, pp. 978–983, Aug. 2016, doi: 10.1002/jrs.4927.

[82] P. R. González, D. Mendoza-Anaya, L. Mendoza, and L. Escobar-Alarcón, “Luminescence and dosimetric properties of CaF2: Ce,Dy phosphor,” *J Lumin*, vol. 195, pp. 321–325, Mar. 2018, doi: 10.1016/j.jlumin.2017.11.050.

[83] A. R. Gee, D. C. O’sheaiand, and H. Z. Cummins, “Printed in Great Bril RAMAN SCATTERING AND FLUORESCENCE IN CALCIUM FLUORIDE,” Pergamon Press Ltd, 1965.

[84] M. Macías, B. Fernández, J. A. Labrador, A. Romero, and J. Praena, “Nanosecond pulsed proton beam: upgrade of the accelerator-based neutron facility HiSPANOS at CNA (Spain),” Jun. 2019, [Online]. Available: http://arxiv.org/abs/1906.05716

9
ANNEXES

9.1 Hunter-Schreger bands

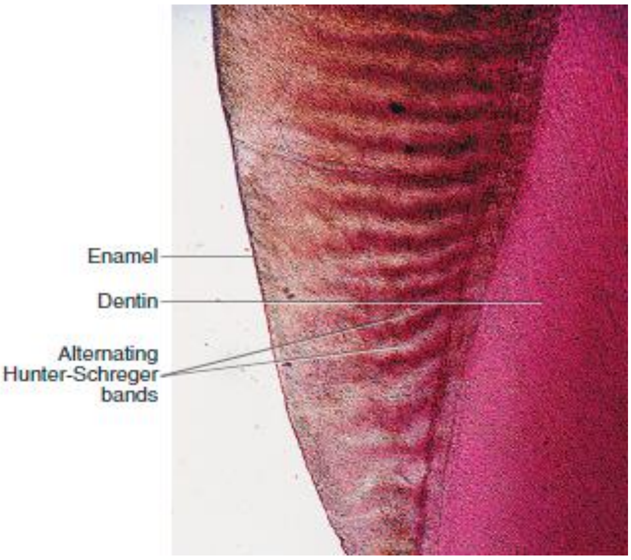

9.2 Buehler isoMET 1000, USA

9.3 Horiba/Jobin-Yvon Xplora, France

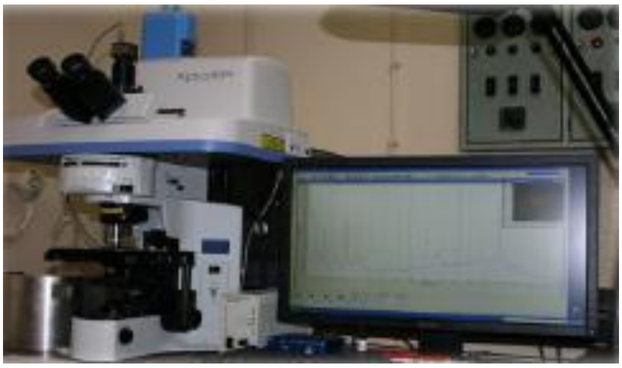

9.4 Sample holder 1, PIGE

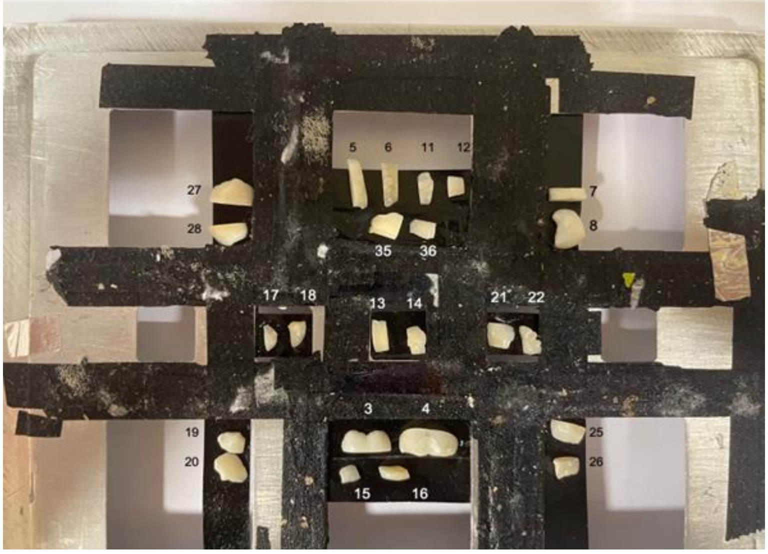

9.5 E Sample holder 2, PIGE

9.6 Sample holder 3, PIGE

9.7 Polarization configurations of Raman spectroscopy

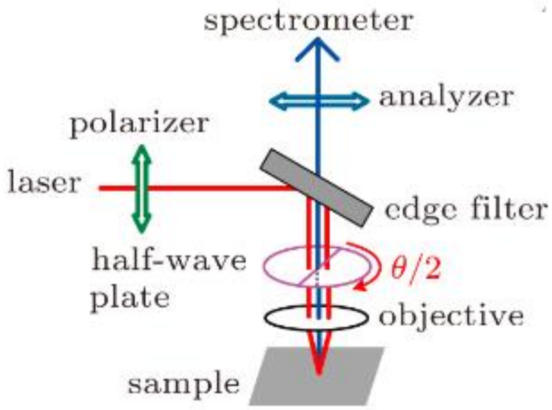

9.8 Polarized Raman spectrum

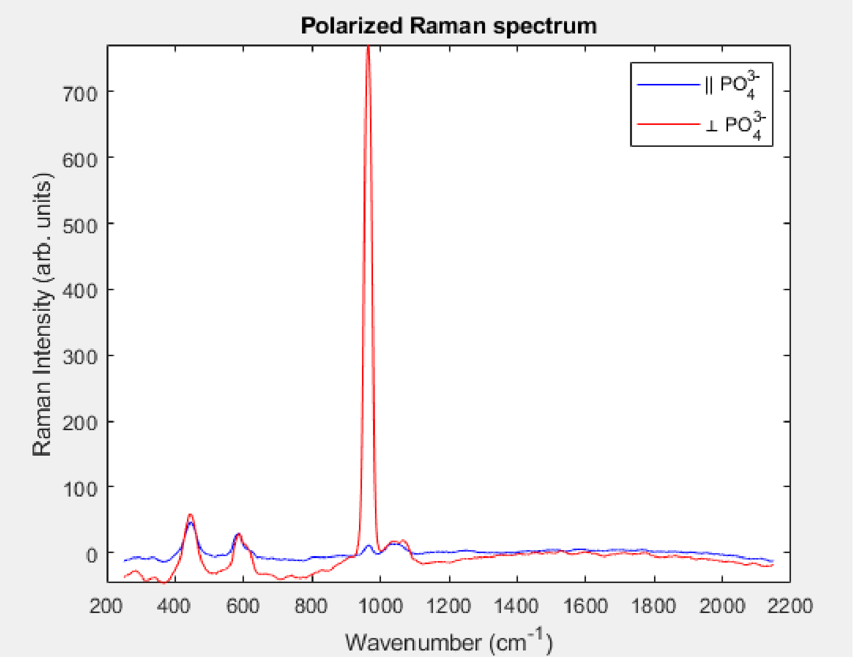

9.9 Smoothing comparison for Raman spectra

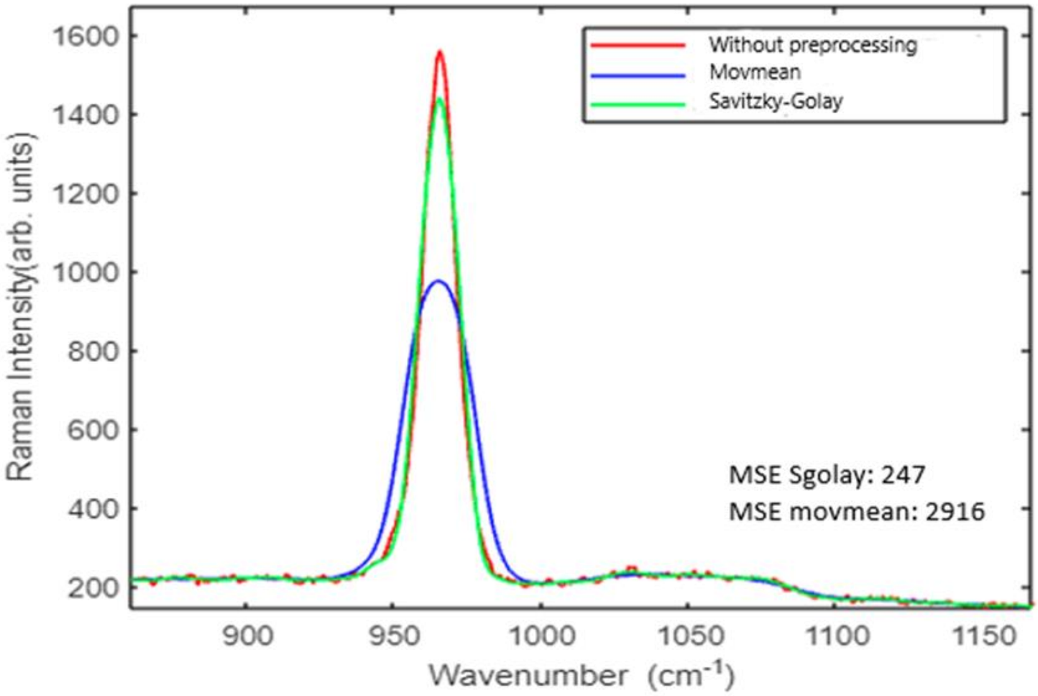

9.10 Difference between control and test spectra

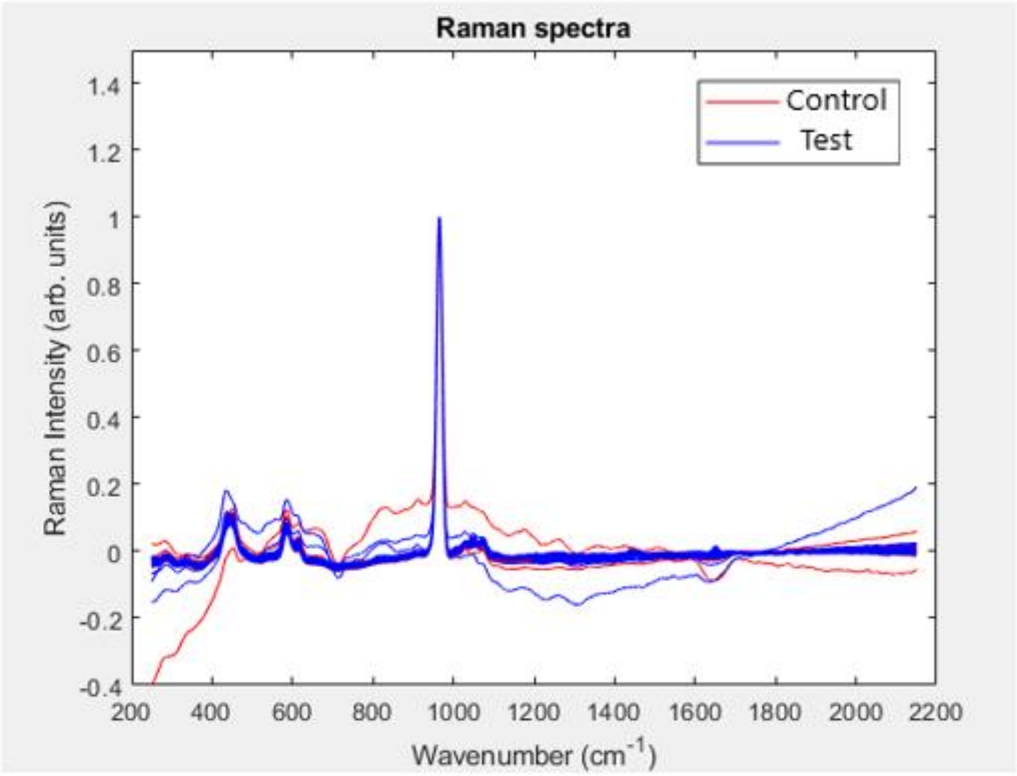

9.11 Gaussian fit of a peak in Matlab

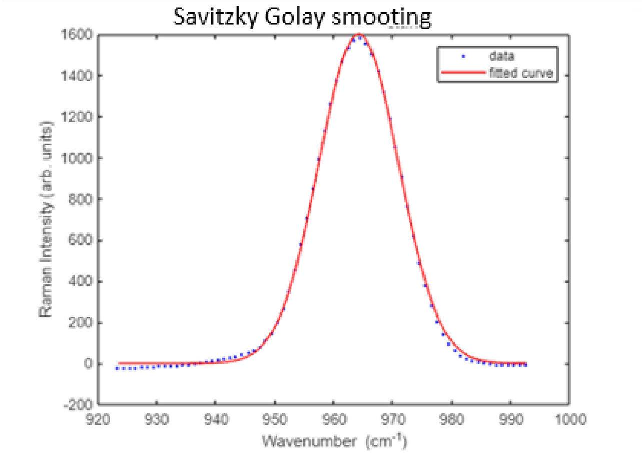

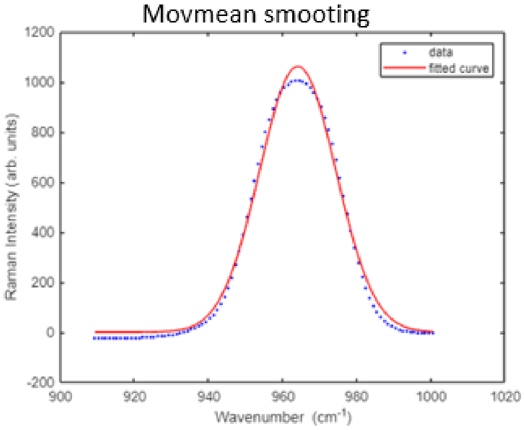

9.12 PCA results for several projections using features

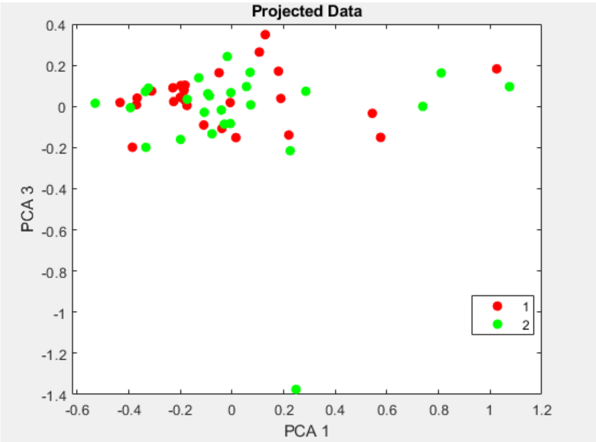

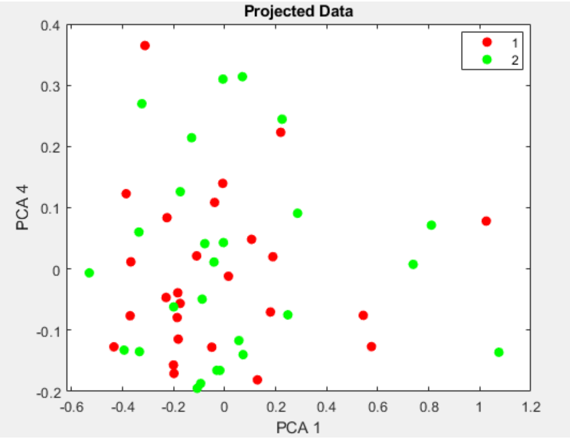

9.13 PCA results for several projections using full Raman spectra

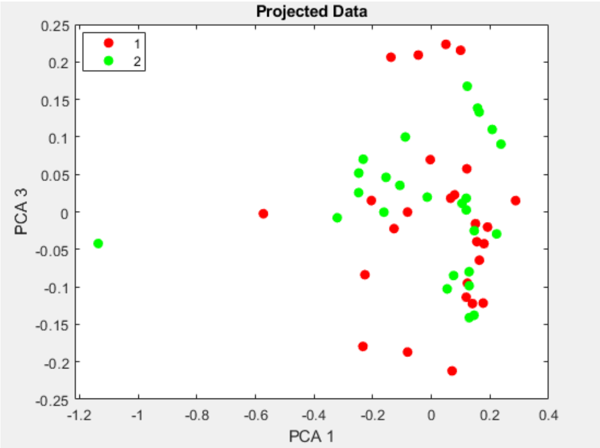

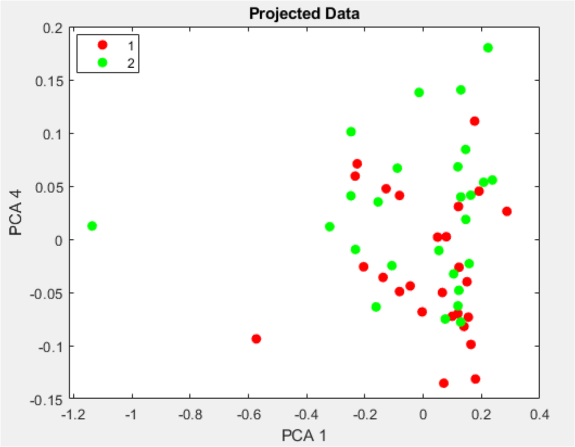

9.14 Features importance from RF classifier using full Raman spectra

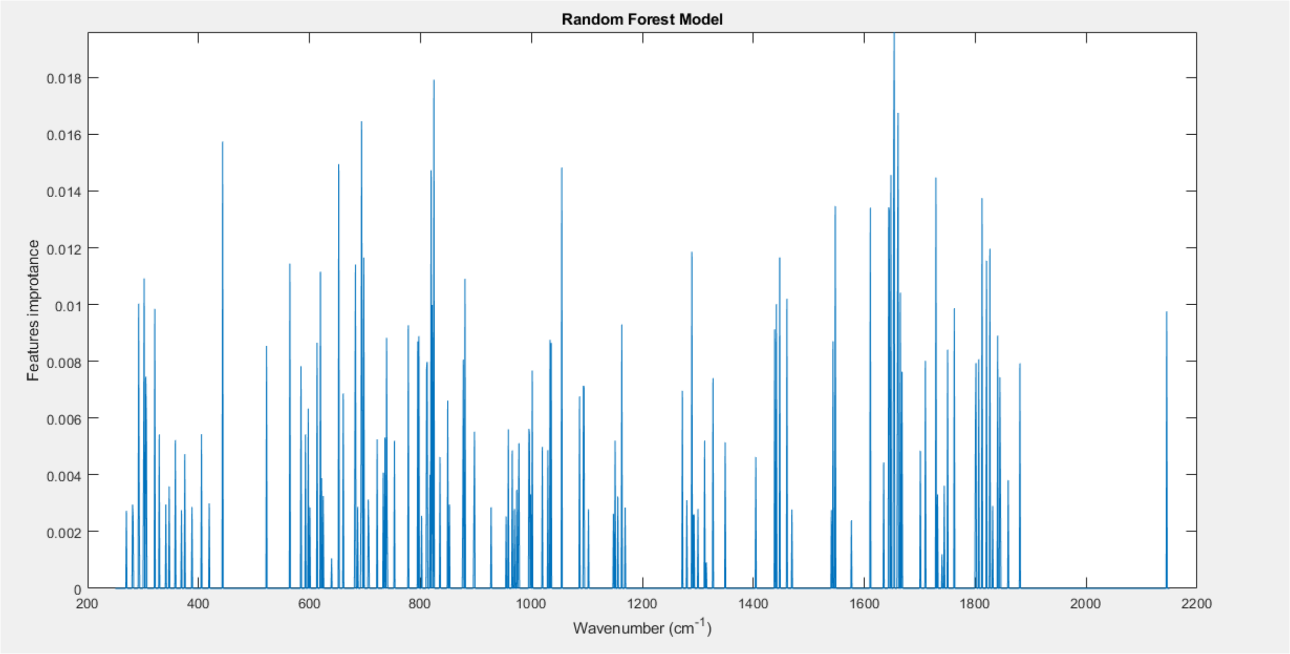

9.15 2D plot of the features importance from RF on a Raman spectrum

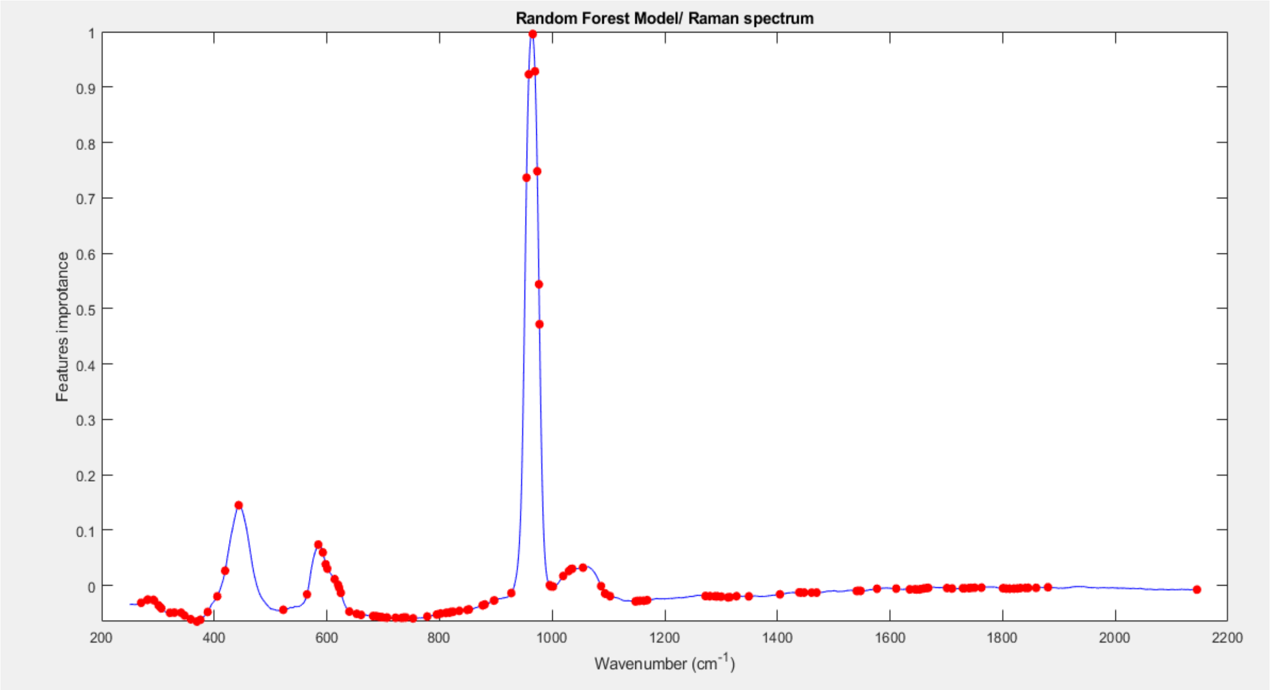

9.16 Coefficient importance for LR using full Raman spectrum

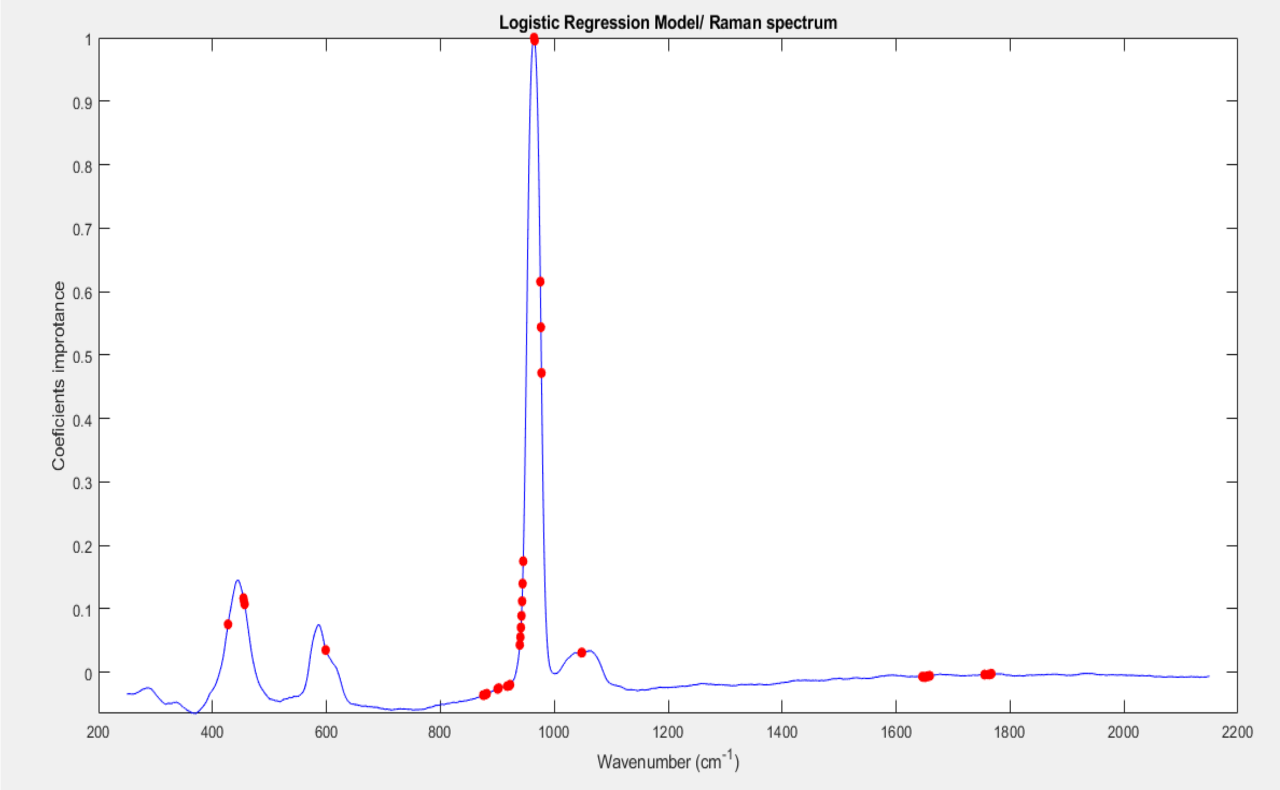

⟨2023⟩ António Delgado Fortes SPECTROSCOPIC EVALUATION OF THE FLUORINE UPTAKE IN HUMAN

NOVA SCHOOL OF SCIENCE & TECHNOLOGY